

SHREWS:

STRATEGIC HIGHLY-COMPLIANT ROVING EXPLORERS OF OTHER WORLDS

LIGHTWEIGHT, MODULAR ROVER CARAVANS FOR GEOPHYSICAL CHARACTERIZATION OF THE PERMANENTLY SHADOWED REGIONS ON THE LUNAR SOUTH POLE AS PART OF THE 2020 NASA BIG IDEA CHALLENGE

THAYER SCHOOL OF ENGINEERING AT DARTMOUTH COLLEGE

February 2020—December 2020

Engineering Team

Adam Gronewold	Team Lead; Ph.D. Candidate—Control, Mechanical Design, Simulation
Christopher Lyke	Eng. Sciences Undergraduate—Mechanical Design, Implementation
Joshua J. Elliott	Ph. D Candidate—Power Electronics, Embedded systems, Simulation
Austin P. Lines	Ph.D. Candidate—Mechanical Design, Terramechanics, Control
Marguerite Généreux	Eng. Sciences Undergraduate—Mechanical Design
Grace Player	Eng. Sciences Undergraduate—Mechanical Design
Philip Mulford	PhD. Candidate—Code Architecture, Control, Implementation
Andrew Skow	Eng. Sciences Undergraduate—Positioning, Thermal Design

Advisor

Dr. Laura E. Ray, Ph.D.	Professor of Engineering—Dynamics and Controls, Mechatronics, Mobile robotics, Terramechanics, Nonlinear estimation
-------------------------	---

Space Grant Affiliation

New Hampshire Space Grant Consortium



Table of Contents

1. Quad Chart.....	1
2. Executive Summary	2
3. Problem Statement and Background	2
4. Project Life-Cycle	4
5. Project Description	4
5.1. Proposed Mission Scenario (ConOps)	5
5.1.1. Traverse Cycle	5
5.1.2. Route Selection and Mission Development.....	6
5.2. Concept Validation with Simulation	7
5.3. Mechanical Design.....	8
5.3.1. Frame, Suspension, & Dynamics.....	9
5.3.2. Attachments.....	10
5.3.3. Motor and Gearbox Selection.....	12
5.4. Electrical Design	12
5.5. Software and Control.....	12
5.6. Required Modifications to Meet Lunar ConOps	14
5.6.1 Dust Mitigation	14
5.6.2 Advanced Materials.....	15
5.6.3. Lunar Electronics	16
5.6.4. Thermal Model.....	16
5.6.5. Teleoperation and Autonomy	17
5.6.6. Comparison to Terrestrial Prototype	18
6. Proof-of-Concept Testing on Earth.....	18
6.1. Locomotion Testing.....	18
6.2. Linking Tests	20
6.3. Testing of Teklam Frame Elements.....	20
6.4. Testing of Teklam Frame Elements.....	21
6.5. Critical Testing not Performed	21
7. Test Results & Conclusions.....	21
8. Safety Plan and Protocols Followed	22
9. Path-To-Flight	22
10. Detailed Timeline	24

11. Detailed Budget	26
Appendix A: References	27
Appendix B: Wheel Design	30
Appendix C: Motor Selection Calculations	32
Appendix D: Connector Arm and Envelope Studies	34
Appendix E: Electrical Diagram	35
Appendix F: Thermal Calculations	37
Appendix G: Teklam Beam Calculations	39
Appendix H: Energy Calculations.....	49

1. Quad Chart

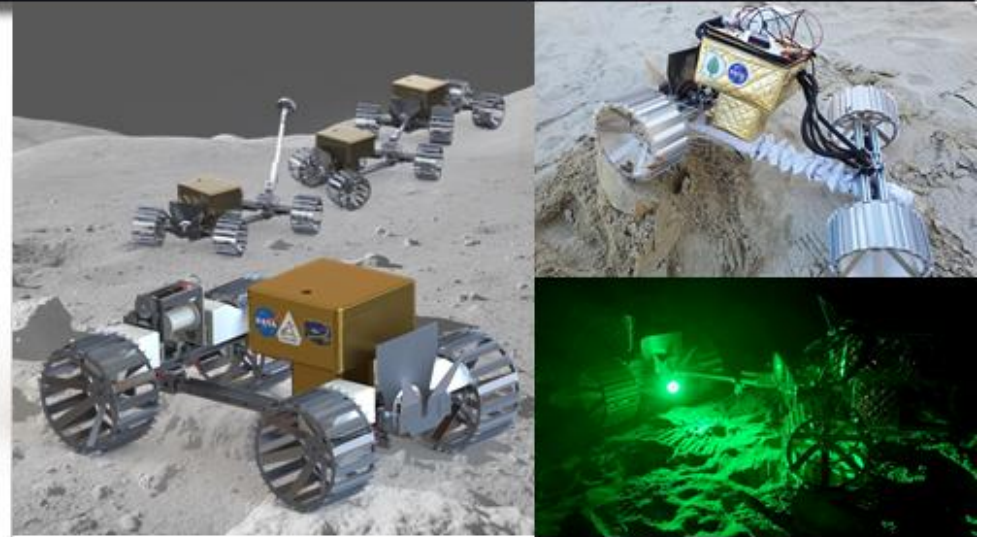


*Thayer School of Engineering at Dartmouth College
Strategic Highly-Compliant Roving Explorers of other Worlds
(SHREWs)*



Concept Synopsis:

SHREWs are modular, collaborative rovers for exploration of the most challenging environments on the lunar surface, namely Permanently Shadowed Regions (PSRs) within craters of the Lunar South Pole. These 4-wheeled, all-wheel-drive, vehicles are highly-mobile units that affect their own extrication from immobilizing terrain via switching between locomotion modes. Caravans of SHREWs provide collaborative deployment and extrication as a system redundancy. SHREWs allow for multiple passages into the depths of PSRs through efficient energy cycling driven by solar power systems along the lit edges of craters. The system can be integrated with concepts presently in development for telecommunications between PSRs and Earth-operators. The innovations of the concept enable high-resolution, geophysical data acquisition required to make in-situ resource utilization (ISRU) practical in these environments.



Innovations

- Novel mobility concept suited for lengthy, partially tethered traverses in PSRs.
- Alternative to traditional rocker-bogie that allows for a variety of driving modalities by independently controlling yaw angles of front and rear axles relative to body. Retains 4-wheel contact uneven terrain.
- Latchment mechanism & end-effector enabling multi-vehicle coordination into larger vehicle system and power transfer between units.
- Expandable mid-frame for push-pull and inch-worm locomotion with just one additional actuator to aid in avoiding immobilization and regaining mobility in friable terrain.
- Highly-efficient packing system allowing the SHREW to compact to 0.21 m³ during launch and extends to 0.33 m³ following deployment.

Proof-of-Concept Testing Results & Conclusions

- Constructed two prototype vehicles and performed testing in sand.
- Capable of traversing rigid and soft obstacles up to 77% of wheel diameter under four-wheel drive mode.
- Low ground pressure with less than 3 cm sinkage in noncohesive soil.
- Verified ability to electromechanically link two SHREWs in both well-lit and low-light conditions.
- Demonstrated ability to modify vehicle wheelbase by actuating the vehicle mid-frame; proves functionality of transport and driving configurations.
- Validated symmetric, asymmetric and parallel off-set steering schemes.
- Verified inch-worming locomotion and collaborative caravan on simulated lunar surface using Gazebo/ROS environment.
- Validated system design parameters and projected energy use on sand and in 0.4 km endurance test on grass.

2. Executive Summary

The Dartmouth Engineering Team presents Strategic Highly-compliant Roving Explorers of other Worlds, or SHREWs, as a solution to the 2020 NASA BIG Idea Challenge. SHREWs represent a novel class of wheeled vehicles well suited for reaching and operating within lunar PSRs in order to gather ground penetrating radar (GPR) and spectrometer data to scout the potential for *in-situ resource utilization* (ISRU) under future Artemis missions.

The SHREW – a four-wheel drive vehicle with advanced mobility stemming from its dynamics—is an underactuated vehicle with independent roll and yaw degrees of freedom for each axle and a variable length midframe. The rover is shipped in a compacted state and expands as it is deployed to the lunar surface. The midframe also enables a push-pull mobility mode to escape from immobilizing terrain, and the vehicle dynamics facilitate four-wheel contact with the lunar surface to comply with terrain elevation variation and to turn with limited scrubbing. A warm electronics box (WEB) shields vital components from the extremes of space. Finally, the SHREW can carry existing NASA-developed payloads for geophysical mapping of PSR stratigraphy and spectral analysis for volatiles. A SHREW forms one element of a robotic caravan whose collective mobile capabilities exceed that of one SHREW. Through biomimicry, we scale collaborative behaviors demonstrated by shrews in nature, which link mouth-to-tail while exploring the forest floor, to that of a *set* of rovers. A physically linked caravan of small rovers allows for safe entry to a PSR through linkages and winches, provides means for communication and data transmission, and enables recharging of individual SHREWs. We develop multi-vehicle linking components that grant individual SHREWs the ability to act independently or collaboratively. This is a behavior yet to be realized for autonomous rovers and for collaborative robotics in off-road environments, making it a compelling candidate for the exploration of PSRs.

We present the design and physical testing of two 21.4 kg terrestrial prototypes and modify vehicle components to develop a 15.3 kg lunar concept that will meet key mission constraints and parameters. We demonstrate the value of SHREW mobility and caravanning mechanisms through high-fidelity simulation of individual SHREWs and SHREW caravans. Physical fabrication and laboratory testing validate linking mechanisms required to operate as a SHREW caravan and show the functional capacity to operate in both high and low light conditions characteristic of PSRs. Physical testing on sand and endurance testing on grass show that the individual SHREW achieves its targeted low ground pressure to maintain mobility and low energy use, and the four driven wheels combined with the actively articulated mid-frame provide the mobility needed to prevent immobilization in PSRs.

To date, our team has performed preliminary testing to advance the concept from an idea (TRL 2) to a physical system validated in a laboratory environment (TRL 4). Similarly, most innovative components of the SHREWs have been built to demonstrate the core, functionally critical aspects of individual SHREWs (TRL 3). This indicates project maturity which has advanced beyond Pre-Phase A Concept Studies to show the concept can meet the high-level needs of stakeholders. The project is nearing the completion of Phase A Concept and Technology Development, expected by mid-March 2021. We have already performed key simulations of high-risk operations and maneuvers; constructed two terrestrial prototypes to demonstrate overall merit of the idea, thus justifying further development; and identified metrics the system must meet in later design phases. In the coming months, our team will undergo a brief design iteration based on additional requirements identified through testing. Additionally, the team will implement software architectures that enable collaborative system functionality and early performance testing will be completed in relevant environments. Invoking our project motto “Ex Umbris, Lux,” our team is confident that SHREWs will light the darkness of PSRs – light for science, light for the next generation of researchers and light on the unknowns of our inner solar system.

3. Problem Statement and Background

Lunar PSRs show great promise for future extraterrestrial exploration as hydrogen rich deposits, identified by projects like the Lunar Orbiter Laser Altimeter (LOLA) and the Lunar Crater Observation and Sensing Satellite (LCROSS), have potential to be utilized in a variety of manners vital to mission operations through ISRU (NASA, 2009). While many studies have nearly universally shown the presence of water ice

in lunar PSRs, the surveys on which they are based are of relatively low resolution. For example, Lucey et al. (2014) produced global surface albedo maps at 1,064 nm with a resolution of 2 km, and found PSRs are brighter than non-PSRs, indicating as much as 14% water frost abundance. More recently, Smith et al. (2017) published several works on “high” resolution digital elevation models constructed from the same datasets at a spatial resolution of 20m per pixel. As NASA and industry partners continue to push the boundaries of space activity and exploration on these fronts, however, water concentrations must be known to higher precision before crewed missions take place. The 2020 NASA Technology Taxonomy, an update to the Technology Area Breakdown Structure (TABS) of the 2015 Technology Roadmaps (NASA, 2020a), outlines key developments required to meet NASA’s near-term objectives. Among the 17 Technology Areas (TXs) identified as critical research and development areas, TX04: Robotics Systems and TX10: Autonomous Systems are of highest importance for our team’s development. Specifically, ensuring stable mobility (TX04.2), developing novel concepts for robotic integration (TX04.6), and rendezvous and docking on the lunar surface (TX04.5) are crucial to constructing high-resolution datasets of the lunar surface and subsurface.

The 2020 NASA BIG Idea Challenge seeks innovative approaches for exploring the Permanently Shadowed Regions (PSRs) and polar regions of the Moon, including exploring and operating inside PSRs and lunar ISRU within a PSR. Inherent in this challenge are engineering requirements for systems and concepts, including mobility in unknown terrain conditions; accommodating extreme temperature variations; operating in a vacuum; operating in the darkness of a PSR; communication constraints; radiation environment; and energy storage constraints. Furthermore, the design concept has value in identifying sites meaningful for lunar ISRU. The resources, stratigraphy, and terrain within PSRs are relatively unknown, requiring innovative concepts and systems that enable us to autonomously explore and operate within these regions. In response, the Dartmouth Engineering Team has developed SHREWs, a rover designed to explore the rim of a PSR and venture beyond the rim while avoiding immobilization. SHREWs can link together in a caravan to descend, explore, and operate within PSRs.

Our team builds on over 15 years of experience at Dartmouth College in the design of lightweight rovers for extreme environments. Three rovers developed at Dartmouth have been fielded in the interior of Antarctica and Greenland over a dozen times since 2005. Through these experiences, we have developed expertise in low ground pressure and low energy design, solar charging for 24-hour operation in summer, terrain diagnostics to avoid incipient immobilization, autonomous control, and mobile science instrument support. We build on this knowledge to develop a rover for the 2020 NASA BIG Idea Challenge.

The primary barrier to mobility near the Lunar South Pole is low soil cohesion, leading to increased likelihood of immobilization for a traditional four-wheel-drive rover. Compounding this issue is the uncertainty of the regolith composition within PSRs, the potential loss of communication upon entering these regions, the energy requirements of autonomous rovers and instruments, and mass constraints for delivery to the moon. With this in mind, we focus our design on robust mobility. We present the conceptual design of a rover that can be used in isolation or link together into a caravan to achieve collective mobility that is greater than that of the sum of the individuals. While we focus on mobility challenges, we are mindful of the additional constraints of operating in the extreme conditions on the lunar surface, including temperature swings, radiation, lunar dust, and vacuum conditions. We develop terrestrial prototype to serve as a proof-of-concept for our lunar design, and we address the technology challenges to scale this prototype for exploring lunar PSRs.

Our development process considered many existing rovers, three of the most relevant are discussed here. Like the Scarab rover, SHREWs are an exploration in vehicle extrication and changing locomotion modes (Wettergreen, 2009). In contrast to Scarab (250 kg), each SHREW is a lightweight platform, well suited for exploration of PSRs and craters on the Lunar South Pole. Additionally, SHREWs maintain a passive suspension through the vehicle kinematics and do not average body pitch angles of rocker suspensions through passive differencing as Scarab does. The vehicle passively complies to changes in the terrain through body roll angles.

NASA’s Volatiles Investigating Polar Exploration Rover (VIPER) is designed to explore the lunar south pole, but unlike SHREWs, it must stay on slopes less than 15° (NASA, 2020b). VIPER is comparable

to an off-road utility vehicle at 430 kg (versus ~60kg for four SHREWs). Each VIPER wheel has two degrees of freedom relative to the body allowing movement in a variety of modes. Actively yawing each wheel in a sequence produces a swimming motion for travelling through fine sand. It drives at similar speeds to SHREWS, between 0.11 and 0.22 m/s depending on tasking. Finally, since VIPER will be operating only 1.3 light-seconds from Earth, near real-time driving is possible, with humans able to directly control VIPER in a manner impossible for NASA Mars rovers.

NASA's DuAxel shares many similarities with SHREWs and was a major inspiration (McGarey et al, 2019). DuAxel is a carrier rover that drives near areas of interest, then deploys two tethered wheeled rovers to travel downhill. It is designed to explore difficult-to-reach cliff faces. These rovers make up DuAxel's two axles when the system is combined, with the body acting as an anchor when the axles are deployed. DuAxel is limited by the length of winch cable that it uses, since the cable provides both a mechanical connection and a link for data and power (Nesnas et al, 2012). These electrical connections require a more sophisticated winch system than that proposed here. While concepts call for their deployment to lunar PSRs (Bandyopadhyay 2020), the system does not appear to be designed for temporally lengthy tethered traverses to survey PSRs.

4. Project Life-Cycle

Project development followed the standard recommended management described in the NASA Systems Engineering Handbook (NASA 2020b). Work done prior to the Dartmouth Team's 2020 BIG Idea Challenge proposal acted as the first system life cycle through Pre-Phase A: Concept Studies. Acceptance as finalists and the feedback provided served as the preliminary Key Decision Point (KDP) in which we were selected for Phase A financial support. A second cycle through Pre-Phase A refined conceptual ideas, solidified parameters critical to concept development, and provided mission scenarios. In early March 2020, our team began Project Phase A: Concept and Technology Development, in which subgroups were tasked with 1) analyzing mission requirements and injecting rigor into baseline mission architectures and 2) component refinement and preliminary design of a proof-of-concept which may validate the Concept of Operations (ConOps). All members were heavily involved in these tasks and assessment of technical risks for the remainder of the project. Feedback from the Mid-Project Report served as both a secondary KDP and a Mission Definition Review (MDR), at which time the team advanced more rapidly through a secondary life cycle at Phase A, completing multiple KDPs internally through June 2020. Construction of terrestrial prototypes began in early July, marking the beginning of later-stage Phase A work, as we hoped to demonstrate merit of the concept by the completion of the Challenge. Meanwhile, a portion of the team remained focused on ConOps. To date, the Dartmouth Engineering Team is nearing the end of Phase A work, having performed rigorous simulation of the mission scenario and assessment of system performance in the face of technical risks on the lunar environment such as power system and thermal system cycling. Baseline performance of physical subcomponents has been demonstrated for individual SHREWs with the terrestrial prototype, justifying future work on the project and merit to the overall concept. Lastly, we intend to perform similar baseline testing of the collaborative aspects of the concept in the coming months. Activities will continue into mid-March under Phase A in response to the Forum and paper review acting as a second, formal KDP and MDR. Pending a "go" indication from key stakeholders, our team intends to pursue Phase B financial support in early spring 2021.

5. Project Description

The system design was driven by constraints outlined by the Challenge, key parameters related to viable mission scenarios, the need for traverses in harsh environments, improved mobility characteristics, technological readiness levels (TRL) of sub-components, and the feasibility of advancing low TRL concepts to flight-ready hardware prior to a human landing on Artemis III in 2024 (NASA, 2020c). The design of two terrestrial prototype vehicles and required modifications for the lunar environment are presented in this section.

5.1. Proposed Mission Scenario (ConOps)

This section outlines a mission scenario for our vehicles based on our investigation of craters of interest, potential landing sites marked by NASA, and water ice concentrations for ISRU. This scenario and its associated slopes, loads, and obstacles provides design parameters for concept development and detailed design of two physical prototypes. Our team is aware of the complexities and variabilities in selecting a true mission plan. This mission scenario will be further refined using the analytical suite of tools available to NASA for mission planning and scheduling at the beginning of Phase B activities. Our mission plan is selected as an extreme, such that deployment to less extreme sites would not require design modifications in the face of the rapid timeline of Artemis.

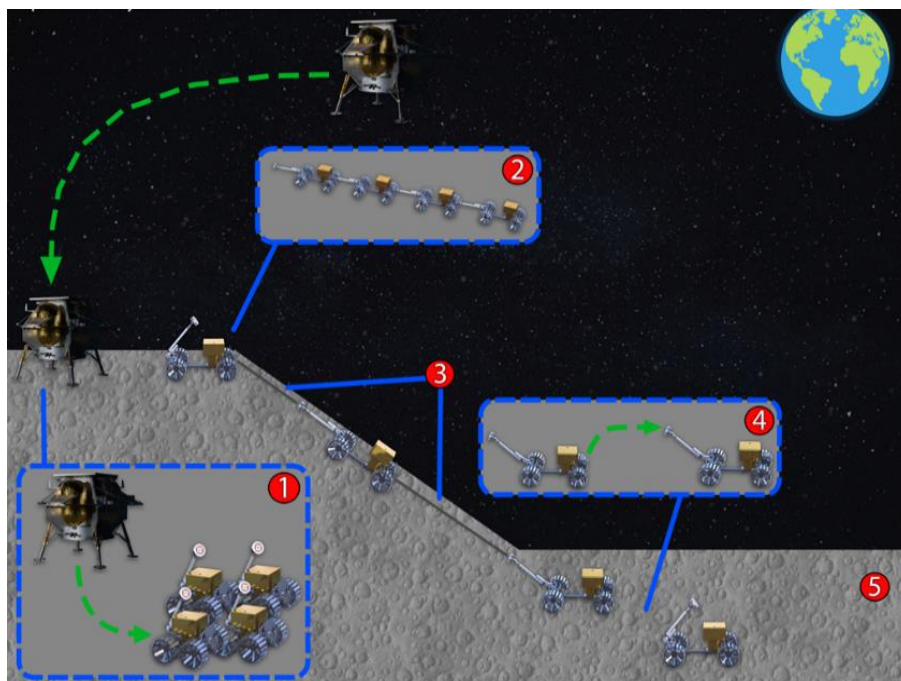


Figure 1: ConOps - Deployment to lunar surface & descent into lunar PSR.

5.1.1. Traverse Cycle

Four SHREWs are delivered to the lunar surface to mount lengthy surveys in and out of lunar craters as shown in Figure 1. At least one vehicle is outfitted with solar panels for energy collection. Two vehicles carry winch mechanisms to lower the caravan into the crater and perform analysis at intermediary strata on crater slopes. Finally, at least one vehicle is capable of detaching from the caravan to operate independently within the PSR.

1. CLPS landers deliver the SHREWs to the edge of a PSR, 100 meters from a crater rim, as specified by the BIG Idea Challenge. During flight, each vehicle is in its transport configuration (Figure 2, left).
2. After descent and landing, the SHREWs exit the lander, expand to their driving configuration, link together to form a caravan, and begin their approach to the crater rim. The solar-paneled vehicle is the back member of caravan, then the two winched vehicles, and the detachable vehicle leads. Upon reaching a peak of eternal sunlight (PEL) on the crater rim, the solar-paneled SHREW maintains its position for the remaining 20 hours of the exploration cycle, charging its batteries while the remainder of the caravan operates in the PSR. This vehicle has a higher energy capacity to recharge the other SHREWs between cycles.

3. The next SHREW unspools its winch to lower itself and the remainder of the caravan a maximum of 3000 meters. The second winched vehicle unspools an additional 3000 meters to deliver itself and the final SHREW to more level terrain ($<15^\circ$). Descent into the crater is aided by gravity, while the descent rate is governed by tension in the cable and braking torques on the wheel motors. Minimal drive energy is needed for winch-aided rappelling of the crater wall. The winched vehicle midway down the slope acts as a radio communications repeater to transmit data out of the crater and back to the CLPS lander, while relaying commands down to the other two SHREWs. The winched vehicles carry low mass, passive instruments like Geiger counters, while the detachable vehicle carries the core scientific instruments: a GPR and spectrometer.

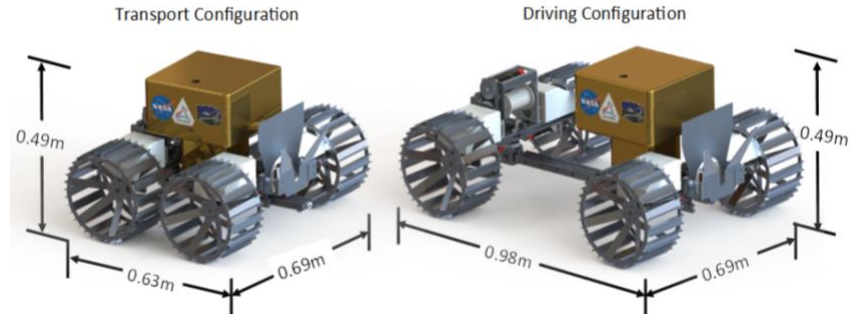


Figure 2: SHREW compacts for transit (Left); extends for driving (Right).

4. At the fully extended length, one or both winched vehicles and the detachable vehicle are inside the PSR. The detachable SHREW delinks and begins its solo exploration deep within the PSR.

5. The solo SHREW completes its traverse, reattaches, and the caravan ascends the crater in the opposite manner it descended, respooling from the bottom up to avoid dragging the cable. Back on the rim, the full caravan reconnects, at which point scientific data takes priority for transmission to Earth while the caravan recharges. The caravan repositions itself on the crater rim and repeats the cycle until the area is sufficiently characterized. From there, the caravan will relocate to another crater.

5.1.2. Route Selection and Mission Development

The mission plan is based on the work completed by the joint working group between the Lunar Planetary Institute (LPI) and Johnson Space Center (JSC) between 2007 and 2012 (Kring & Durda, 2012). Our site selection follows their methodology, including pre-processing, classification and priority weighting, and post-classification analysis. Pre-processing comprises gathering map data of hydrogen concentrations, either in crystalline form or as saturated

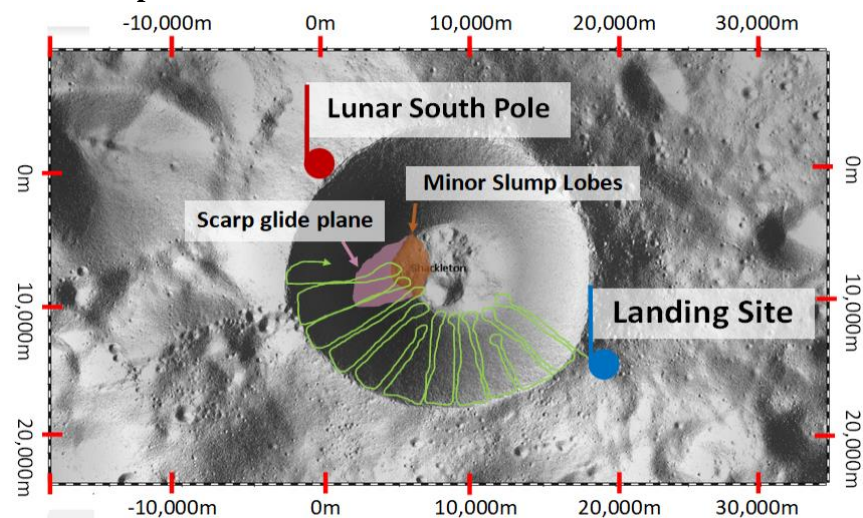


Figure 3: Primary mission traverse at Shackleton Crater.

regolith silicas, temperature data, slope data, solar visibility, and additional volatile concentrations. A combination of LOLA data, LCROSS data, and volatile maps visualized on JPL's MOONTrek informs site selection (Clark, 2009, NASA, 2020d). Key volatiles include hydrogen, iron oxide, clinopyroxene, olivine, orthopyroxene, and plagioclase. Mission weighting is also based on potential to reveal information about the age or history of the inner solar system, with priority for sites with $>50\%$ solar visibility throughout the lunar solar cycle on the PSR edge. From this, we developed a short list of sites based on this weighted metric. These sites included Shackleton, Malapert F, Amundsen, Faustini, Cabeus B, Haworth and the southern face of Malapert Peak. We developed goals for each site and considered viability of our concept for each site.

The selected landing site targets the rim of Shackleton Crater at roughly 25 km from the Lunar South Pole as shown in Figure 3. Traverse cycles are shown broadly by the green line. The surface of Shackleton Crater is estimated to be one of the oldest surfaces on the Moon (~3.6 billion years old), and characterization of this surface is equally valuable for ISRU as it is for improving geological models of the development of the lunar surface. Craters of similar size and slope tend to have similar morphologies, distinguished by relatively flat floors and slump lobes at their bases. Stratigraphy of the crater and study of the crater's age may be improved by analysis of scarp glide horizons and transition regions into slump lobes, as these surfaces have likely been exposed to damaging solar wind for shorter periods (Spudis et al., 2008). Likewise, these surfaces may prove meaningful to understanding the bombardment history of the inner solar system (Kring & Durda, 2012). This will be a primary focus of the mission alongside stratigraphy and volatile characterization.

5.2. Concept Validation with Simulation

Our concept posited that a robot with independent roll and yaw degrees of freedom for front and rear axles combined with an internal joint for expansion and contraction, and intervehicle linking mechanisms would enable mobility modes that reduce potential for immobilization in soft terrain. To explore these concepts, we used a high-fidelity robotics simulator, Gazebo. Its physics simulator includes rigid body dynamics, collision detection, graphical rendering and more. Custom terrain models can be implemented to supplement its standard friction model. Robot Operating System (ROS) is a software framework used to speed up design, analysis, and software development for real and simulated robots. It provides a communication system for different program nodes (standalone executables) to send and receive messages (e.g. allowing a vehicle controller node to send commands to a motor interface node). ROS and Gazebo combined allow for robotic software development and hardware design without physical iteration. They also allow for testing in inaccessible environments, such as the Moon, where certain details of the environment, such as gravity, are difficult to physically simulate on Earth. Here, we use ROS and Gazebo to evaluate the mobility concepts for individual and caravans of SHREWs proving viability of the conceptual design prior to the completion of a physical prototype.

Figure 4 shows a simulated SHREW in the ROS/Gazebo environment rolling over simulated, friable lunar terrain possessing limited trafficability. In this single-SHREW simulation scenario, the rover is unable to move forward through four-wheel drive. Much like the larger, heavier Scarab rover, the SHREW can lengthen and shorten its wheelbase in order to move across terrain in an inchworm-like manner (Creager et al., 2014, 2012); Moreland et al., 2011). Inchworm movement is achieved by alternately driving the front and rear wheels while contracting and lengthening, respectively, the midframe joint to allow the vehicle to “inch” forward. The time-domain simulation plots of wheel speed and midframe linear position shown in Figure 5 denote forward progress. For simplicity, two wheels on the left side of the vehicle are shown along with the position of the midframe joint. An additional adaptation required by the underactuated system is that the two wheels on each axle are driven differentially to keep the axle pointed in the desired direction during each stage of the motion. Simulations show that simply driving them uniformly results in the axle turning into areas of lower traction, and the vehicle moving off the desired heading. The synergy between this mobility mode and allowing compact storage for flight further justifies its inclusion in the design concept.

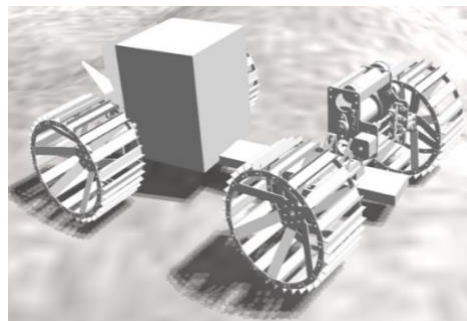


Figure 4: A simulated, winch equipped SHREW travels over undulating terrain

Given the passive yaw joint at each axle, SHREWs can steer and drive in many ways, one of which is crab movement. Crab movement is achieved by parallel axles that are not perpendicular to the body as shown in Figure 6. Crab movement is desirable when repeated passes through the same wheel tracks can decrease mobility. Multiple linked SHREWs can use crab movement when descending slopes to prevent material dislodged by one vehicle from striking another downhill. While individual SHREWs can steer in a conventional manner by pointing the front axle in the desired direction while forcing the rear axle yaw angle to zero, crab movement is achieved by commanding the rear axle to a non-zero angle while the front axle seeks the desired heading.

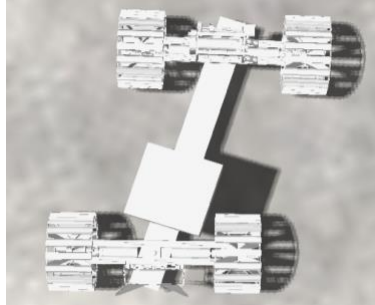


Figure 6: Crabbing motion of a single SHREW.

approaches for such a vehicle are identified before hardware is built. Figure 7 shows a train of two linked SHREWs in Gazebo and provides time histories of the yaw angle of each axle during linked path following.

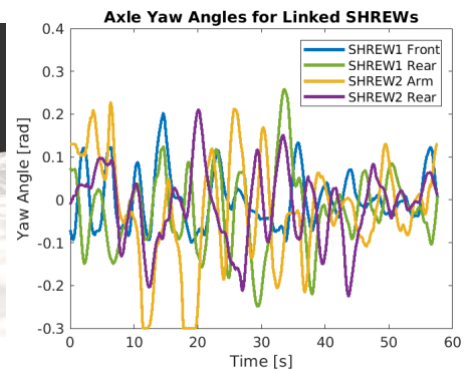
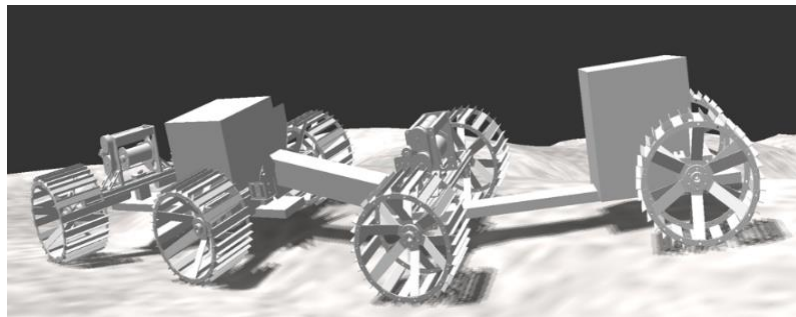


Figure 7: Two SHREWs linked via linking arm travel together (Left). Time histories of front and rear axle yaw angles during path following (Right).

5.3. Mechanical Design

ROS/Gazebo simulations along with mission scenario requirements and BIG Idea Challenge specifications provide the set of design requirements for a single SHREW shown in Table 1. In this section, we present the design of a terrestrial SHREW followed by modifications required for meeting lunar exploration requirements. The SHREW design solution is a four-wheel drive vehicle with translational and

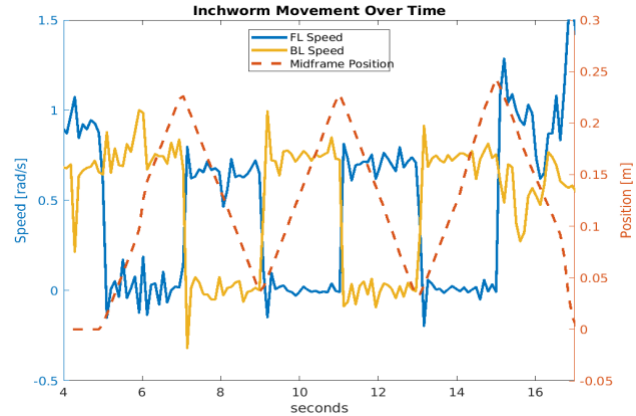


Figure 5: Inchworm mobility mode across friable terrain with low trafficability.

rotational degrees-of-freedom of its three rigid bodies: the front and rear axles and the midframe; a warm-electronics box (WEB) mounted on the midframe; a winch and/or arm for coordination and caravanning; and payload space on each side of the front and rear axles. Figure 8 shows a cross-sectional view.

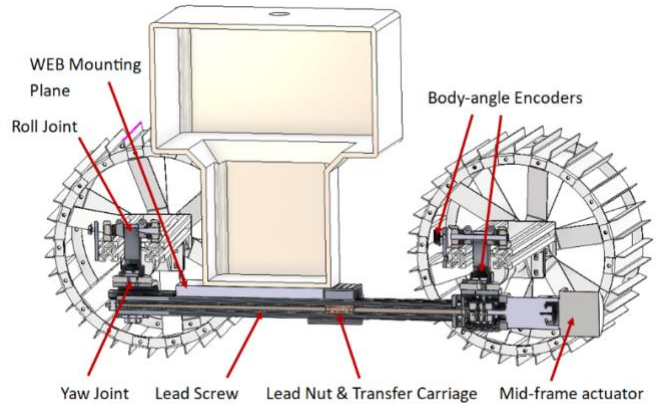


Figure 8: Section view of the vehicle's actuated mid-frame

Table 1. Design requirements for SHREWs				
Requirement	Lunar rover	Terrestrial prototype	Justification	Quantification
Mass	≤ 15 kg	≤ 20 kg	BIG Idea specifications Low ground pressure	Measure using scale
Ground Pressure	≤ 0.85 kPa	< 2.20 kPa	Sinkage in regolith	Determined from sinkage
Compacted length	< 0.6 m	< 0.7 m	Minimize launch volume	Physical testing
Extended length	> 0.9 m	> 0.9 m	Inchworm mode	Physical testing
Maximum speed	0.42 m/s	0.5 m/s	Mission requirements and battery capacity	Physical testing
Volume (compacted)	< 0.25 m ³	< 0.25 m ³	Launch cost	Physical testing
Internal Temperature Limits	-40°C to 60°C	N/A	Protection of vital electronics	N/A
Endurance	15 km	N/A	PSR geometry	Testing and calculation
Slope	Up to 15°	Up to 15°	Mission requirements	Limit testing on slopes
Mid-frame actuation Force	> 24.2 N	> 294.0 N	Mass of frame linkage, wheels, mass density of regolith	Loading cell

5.3.1. Frame, Suspension, & Dynamics

Each SHREW has five rigid-body degrees of freedom, as shown in Figure 9, along with four wheel degrees of freedom. Two axles are positioned on either end of the mid-frame as mounting surfaces for wheel motors, instrumentation, and operational mechanisms (winches or elements of the linking arm system). Each axle has a passive roll and yaw degree of freedom. An actuated, prismatic degree of freedom between front and rear axles allows the vehicle to modify its length. Coordination of this mid-frame translation with wheel actuation allows the vehicle to push or pull its front or rear axle if immobilized by soft terrain or high-centered as simulated in ROS/Gazebo. Types and limits on the as-designed joints are shown in Table 2. The mid-frame is comprised of a motor and lead screw attached to one axle assembly, which drives a lead nut and transfer carriage attached to the other axle assembly (Figure 8). When actuated, force is directed translationally to drive the vehicle halves apart (Table 2). The wheel design is provided in Appendix B.

5.3.2. Attachments

The mid-frame is sized to support the weight of the WEB. Surfaces on either end of the vehicle provide mounting points for operational hardware, such as the winch described in the mission scenario, the linking components that allow for coordination of multiple vehicles, and scientific instrument payloads. Instruments, such as micro-GPR, spectrometers, and cameras, may be placed in four locations as shown in Figure 10.

Joint Name	Joint Type	Joint Limits
Front and rear roll joint F_{Roll}, B_{Roll}	Revolute	$\left[-\frac{\pi}{6}, \frac{\pi}{6}\right]$ rad
Front and rear yaw joint F_{Yaw}, B_{Yaw}	Revolute	$\left[-\frac{\pi}{4}, \frac{\pi}{4}\right]$ rad
Mid-frame Joint	Prismatic	$[0.2, 0.9]$ m

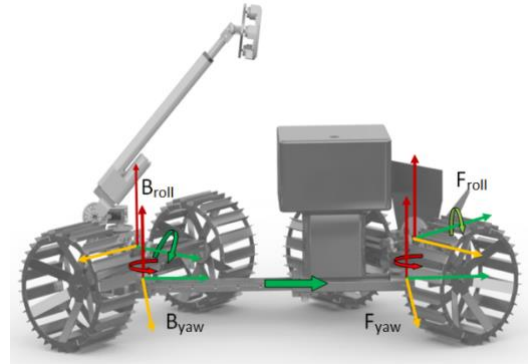


Figure 9: Degrees of freedom of a SHREW robot.

Linking Arm and Envelope

The linking arm allows two SHREWs to semi-autonomously connect and disconnect when positioned at varying distances, heights and angles. This connection is both mechanical and electrical: when mated, the units function as a larger caravan with the ability to transfer power between each module.

For the terrestrial prototype, we selected a rod linear actuator with potentiometer feedback to allow the arm to extend outward in the direction of the other vehicle. The actuator can apply 667 N of dynamic force with a stroke of 30 cm, enabling the two SHREWs to mate when they are positioned between 50-80 cm apart. Based on the mass of this actuator and the estimated mass of the end effector, two high-torque servo motors (Hitec D645MW) and 7:1 gearboxes were selected to control the arm's pitch and yaw movement. The end effector plug features a custom aluminum mount and a ball joint linkage. The ball joint allows the plug to rotate so that it can mate when the SHREWs are not directly facing each other. A circular aluminum plate is attached to the ball joint linkage and serves as the strengthened backing to the spring-loaded plug made of 3D-printed PLA. In order to transfer power, the plug has copper busbars that protrude out of the plastic in a radially symmetric pattern similar to a coaxial power connector. When the plug is inserted into the linking envelope, four embedded wave springs provide ~66 N of contact force between the busbars on the plug and the busbars in the envelope receptacle. The final linking arm and end effector assembly is shown in Figure 11. The envelope is fabricated from aluminum sheet metal and acts as a "funnel" for the linking effector (Figure 12). An FEA simulation used in the envelope design is provided in Appendix D.

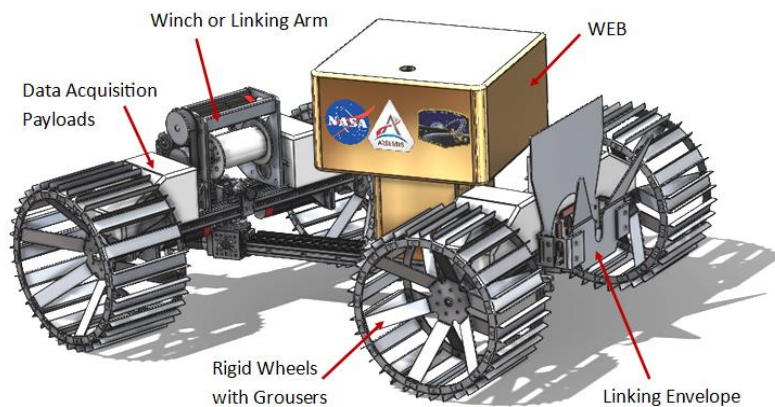


Figure 10: Attached features of SHREW robots

The envelope is fabricated from aluminum sheet metal and acts as a "funnel" for the linking effector (Figure 12). An FEA simulation used in the envelope design is provided in Appendix D.

Winch

The terrestrial prototype winch uses a spool and actuated levelwind to distribute 150 meters of number 12 stranded 1/16" Dyneema rope evenly across a 5.45 cm diameter drum. The rope is coated with Samthane for a low-cost solution with high abrasion and tension fatigue resistance (R&W Rope, 2020). The design is simplified from what would be required for the lunar mission scenario to remain within budget constraints. Lower lunar gravitational forces allow for 3000 meters of a size 207 Aramid (Kevlar) cable with a breaking strength of 284 N, 0.46 mm diameter, and 0.71 kg total mass while fitting within the same winch drum volume. Figure 13 shows the assembled terrestrial prototype winch.

Payloads

SHREWs can accommodate a payload of scientific instruments of one to five kg suspended from the mid-frame or mounted atop either axle. Among instruments of interest, Ground Penetrating Radar (GPR) is one of the most important instruments for mapping the stratigraphy of PSRs in order to study the composition of the regolith to depths of over a meter. Kim et al. (2005) developed a miniaturized GPR unit optimized for lunar prospecting with TRL 4. This GPR system consumes 1 W of power, has a mass of 45 g, and operates at 800 MHz providing signals to 10m depth with 15 cm resolution. The system incorporates two Bowtie antennas, and the required separation between the transmit and receive antennas can be rigidly maintained within the length of the SHREW. Additionally, the expansion and contraction of the chassis allows variable distance between transmitter and receiver such that a lower frequency GPR system could be implemented to achieve a deeper penetration depth when transmit/receive antenna are separated by more than ~25 cm. GPR can determine relative dielectric permittivity, which is an indirect indication of density when no liquid water is present; absolute permittivity is identifiable if a point target is buried beneath the transect, and geologic structure can give clues as to the nature of the regolith (Arcone, 2020). RIMFAX, NASA's GPR on Perseverance, could also be reused for deployment via a SHREW. This GPR has a mass of under 3 kg, a volume of 19.6 x 12 x 6.6 cm, consumes 5 to 10 W and penetrates to a depth of 10 m using a variable frequency GPR (150 MHz to 1.2 GHz) (NASA, 2020e). A variant of Perseverance's SHERLOC instrument - a spectrometer for detecting organic molecules may also be accommodated. SHERLOC's as-designed mass, power, and size for the Mars mission are 3.11 kg, 16.6 W, and 26 x 20 x 6.7 cm, and a PSR variant can eliminate the imager to reduce power, mass, and size (NASA, 2020e).

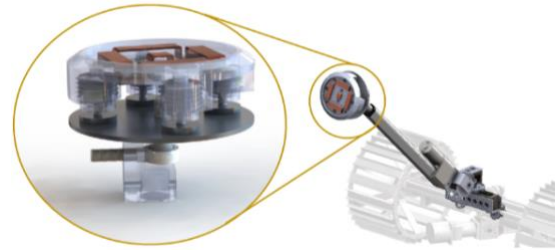


Figure 11: Linking arm and end effector

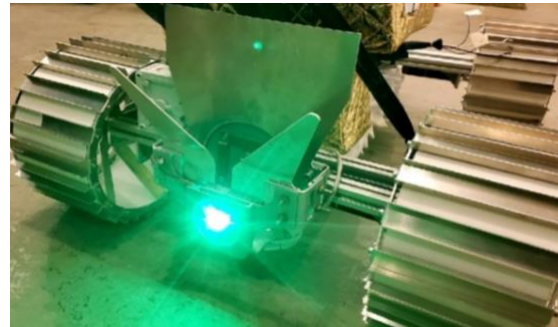


Figure 12: Final envelope with embedded LED for color tracking



Figure 13: Winch mechanism for Earth prototype.

5.3.3. Motor and Gearbox Selection

We size our motors for slopes of up to 15° , and we include a winch to aid in ascent or descent of slopes greater than 15° , as calculations show that for slopes beyond this wheel friction alone may be insufficient. We assume a rolling resistance of 30% of normal force corresponding to rigid wheels in plastic, uncompacted regolith, based

on a modified Bekker approach to evaluate terrain resistance (Carrier, 1996). We also assume a maximum steady-state speed of 0.5 m/s. The required motor torque-speed and power characteristics, for both the lunar vehicle and the terrestrial prototype, are shown in detail in Appendix C. Given a 27.4 cm wheel diameter and 24V DC operation for the Earth prototype, the selected ElectroCraft brushless DC motor, LRPX40, with a 63:1 gearbox (ElectroCraft, 2020) allows continuous ascent of slopes of 15° (motor output of 4.5 Nm) and intermittent towing of another vehicle up the same slope (motor output of 9.2 Nm). The motor characterization is shown in Figure 14. Due to the COVID-19 pandemic, we were forced to select an in-stock gearbox with sub-optimal efficiency, as lead times for custom gearing with higher efficiency were too long.

5.4. Electrical Design

Each SHREW includes a primary and secondary Arduino Due board, as well as one Raspberry Pi model 3B+ connected to the connective arm assembly. One Due outputs commands over serial to two SBL2360T two-channel Roboteq motor controllers to control the drive motors and maintain vehicle heading. The second Due controls the winch motor and midframe joint motor and has capacity to control payload operation. Each Due has a six channel encoder shield, with four encoder channels to measure wheel speed, four channels to measure roll and yaw angle of each axle relative to the mid-joint, and one channel for the winch motor encoder. For winch levelwind control, the secondary Due uses a ROB-12779 stepper driver to actuate the winder. Two Ultralife UBBI-13 batteries provide 576 Wh of energy (Ultralife, 2020). The wiring diagram and embedded hardware architecture for the system can be found in Appendix E.

5.5. Software and Control

The software architecture for the terrestrial prototype is decentralized to enable rapid development of individual sub-systems. The architecture uses the two Arduino Due boards combined with brushless motor controllers. The rover with the linking arm makes use of a Raspberry Pi 3B+ to interface with the camera module and handle image processing. One Due has direct control over all four drive wheels via two of the Serial outputs on the board. The second Due commands the winch, mid-frame joint, and linking arm by way of the Raspberry Pi.

The locomotion of the terrestrial vehicles is governed by an embedded speed controller for each motor (four inner

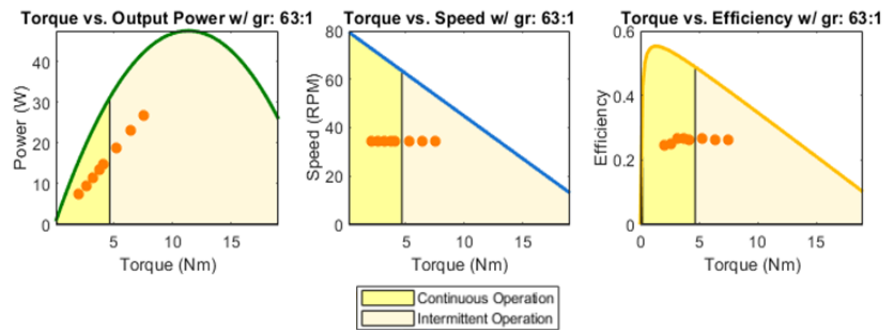


Figure 14: Motor characterization for 20kg Earth vehicle with a 63:1 LRPX40 brushless gearmotor. The orange dots denote operation parameters derived from the mission scenario.

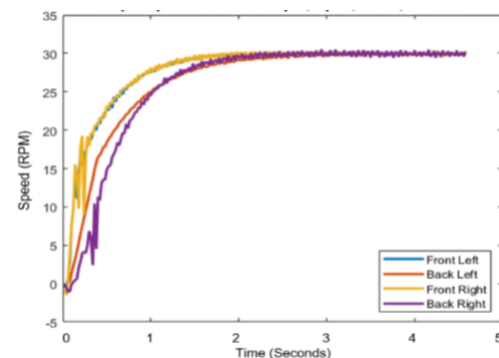


Figure 15: Motor speed response to a reference step input of 30.0 RPM.

loops of a feedback system) with outer control loops independently maintaining a commanded yaw angle between the mid-frame and each axle. As described in Section 5.2, we have also implemented controllers in ROS and Gazebo for complex maneuvers, such as inch-worming and driving of physically linked vehicles. We anticipate that in practice, the caravan will operate with mid-level autonomy, relying on a human supervisor to initiate the action, and on-board controls dictating the motion of the individual rovers and caravan based on simplified mobility metrics.

The lowest level of locomotion control is closed loop control of motor speeds using proportional-integral compensation. Figure 15 shows the benchtop assessment of these control loops, which provide zero steady-state error and an average settling time of just under 2 sec. The outer loops are proportional

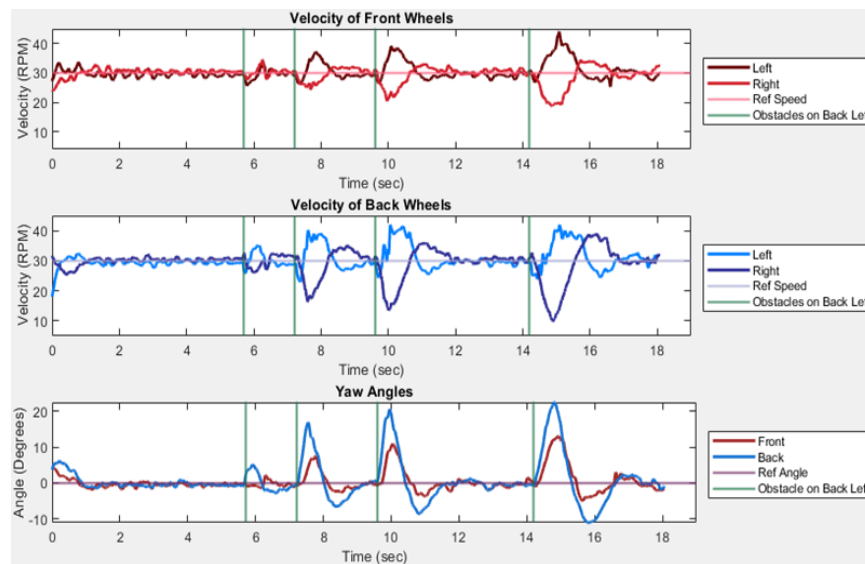


Figure 16: Yaw angle control responding to obstacle events in front of single wheel.

controllers that respond to changes in body yaw angles. When the vehicle encounters an obstacle or has differential resistance between the left and right wheels, the event causes these passive joints to diverge from their reference yaw angle. The outer loop detects the yaw angle error using yaw encoders and increments the commanded motor speed on one side while decrementing the commanded speed on the other side to maintain a commanded yaw angle. Figure 16 illustrates this compensation for independent yaw angle control of each axle. The system is tuned such

that, for large yaw angle errors, wheels on the same axle can move in opposite directions to allow repositioning the axle while the vehicle is moving very slowly. This prevents excessive wheel slip that could lead to soil excavation and immobilization through high centering. The yaw angle controller also functions to command a trajectory with a specified radius of curvature through changing front and rear yaw angle commands.

While the roll and yaw degrees of freedom provide for agile turning, maintaining wheel contact with uneven terrain, and enhanced mobility, they also serve a larger purpose, namely detection of changes in terrain resistance and inconsistent resistance from left to right side of the vehicle. The latter condition can result from a localized patch of heterogeneous terrain. In accommodating for terrain heterogeneity, control commands in wheel speeds, variation in motor currents, and time histories of roll and yaw angles enable the vehicle itself to serve as a proprioceptive sensor of terrain conditions. In the coming weeks, our team will implement a similar reactive control law to change the wheelbase of the vehicle by actuating the mid-frame, in response to difference in roll angles or high terrain resistance detected through monitoring motor currents. Likewise, push-pull locomotion will be implemented as simulated in Gazebo/ROS and testing will be performed to assess the vehicles ability to extricate itself from immobilizing terrain.

Connector arm function is controlled by the Raspberry Pi. Because of the camera's limited field of view, the arm first goes through a sweeping procedure from left to right until the colored object is in its frame. Using the OpenCV computer vision library, the Raspberry Pi locates the circular disk or LED based on its HSV color profile and sends the coordinates of the object to the Arduino board, which orients the arm to the desired position and extends the linear actuator based on the object's radius. All object tracking code is written in Python, and the arm control is programmed using the Arduino programming language, a C++ variant.

5.6. Required Modifications to Meet Lunar ConOps

The lunar concept follows directly from our terrestrial prototype, while considering the many required changes for operation beyond Earth. The overall size and mass are reduced to meet the design constraints, and two key aspects of the lunar environment (dust mitigation and thermal protection) are considered.

5.6.1 Dust Mitigation

Dust mitigation is a critical factor in the success of our lunar rover, as our design relies on moving parts. Excluding those parts that can be placed in dust-tight boxes, the dust mitigation systems are directed towards the mid-frame gantry, winch, motors, and linking arm.

Mid-Frame: The mid-frame joint mechanism hangs between the two axles and is subject to the dust disturbed by the wheels. While larger pieces of regolith are likely unable to rest on the joint, finer soil (<1mm) and dust (<20 μm) particulates can contaminate the mechanisms within the joint and hinder its function (Noble, 2009). The major locations of contamination include bearings, tracks, and the lead screw. Our dust mitigation solution lies in the historically successful beta cloth, a tightly woven, Teflon-coated fabric that currently protects the International Space Station (ISS) and parts of the Curiosity Rover and was previously used extensively on the Apollo Missions to the moon (Bron Aerotech, 2020). Beta cloth has been proven to resist contamination by lunar dust and has been studied extensively by NASA. Beta cloth is resistant to permeability by lunar regolith particulate greater than a few μm in diameter, which is well within the reasonable range for what is expected for the lunar regolith (Christofferson et al., 2009). It is also resistant to damage from abrasion and UV light, and functions in temperatures between -272°C and 650°C , which meets lunar application requirements (Finkenor & Dooling, 1999). Beta cloth is a flexible, durable, and relatively lightweight option at 0.0237 g/cm^2 (Finkenor and Dooling, 1999) that is ideal for protecting the mechanisms of the joint. For this application, the beta cloth can be sewn into a continuous sleeve, matching the maximum length of extension for the joint, and would be fairly tight around the joint to allow for motion in the joint but prevent bunching that would interfere with operation. The terrestrial prototype mimics this function with sewn canvas. The layers will follow a similar pattern to those used in the spacesuits for the Apollo 11 missions, emphasizing abrasion and thermal radiation protection, e.g., using Teflon T-164, Beta 4484, Teflon T-164, Beta 4484, and Aluminized Kapton film/beta marquisette. The repeated layers of T-164 and Beta 4484 provide abrasion resistance and dust protection, and the Aluminized Kapton film/beta marquisette provides thermal radiation protection.

Winch: The winch mechanism is prone to contamination due to the deployment and retraction of the cable between the rover modules. The cable material is resistant to abrasion, but preventing dust buildup is critical (Christofferson et al., 2009). As the winch drum and motors are housed in a container that is entirely sealed except for the cable opening, only the cable must be decontaminated. Figure 17 shows a CAD model of the winch dust mitigation concept. As the winch draws the dust-coated cable in, it passes through a cleaning mechanism, envisioned as an open cage-like structure with Zephyr Fiberglass and Escoda nylon brushes lining the interior. These brushes are a potential cleaning tool for lunar solar panels and remove up to 90% of particulate with a swiping motion (Gaier et al., 2011). The brushes are durable while also mitigating damage to delicate solar panel surfaces, so they would likely be suitable for this application. By drawing the cable through this mechanism, the brushes mimic the cleaning motion and remove particulates before the cable enters the sealed box. The open cage on the exterior also prevents the buildup of dust within the brush mechanism itself, thereby preventing extensive dust contamination.

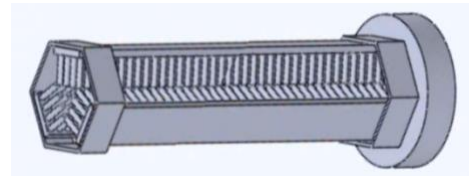


Figure 17: Concept design for winch dust mitigation

Motors: The motors are at risk for lunar dust contamination due to their proximity to the wheels, which could reduce efficiency and functionality. To prevent this, the motors are housed in a sealed casing that leaves only a floating sealed bearing for the shaft to exit the box and connect to a shaft collar, which would be sealed with PFPE grease. A variant of this method has shown promising results with the VIPER

rover module, using a flexible fabric that encapsulates the entire wheel module, including the suspension and motor, with a floating sealed bearing for the shaft to exit (Tabor, 2020). For the SHREWs to function, only the motor housing requires protection. Enclosed absolute encoders for motors of a variety of resolutions are available to ISO and AS9100 standards and have already reached TRL 9 (Gurley Precision Instruments, 2020).

Linking Arm: The linking arm faces similar contamination modes as the mid-frame, with an exposed electrical connection mechanism to link multiple SHREWs. We present two potential solutions to dust mitigation for the arm. The first solution uses the same brushes as for the winch cable but uses them to swipe off the surface. The Zephyr and Escoda brushes have been shown to remove 80 to 90% of the dust. Provided the connection plate is made of a similar material to the thermal control surfaces AZ93 and AgFEP used in the testing simulation, this application could provide a viable solution (Gaier et al., 2011). Alternatively, as dust particles carry a charge, another study suggests the use of an electric curtain to repel the charged dust from the surface. This concept is a promising option to mitigate the dust contamination on the surface of the connector but is still under development. The robot naturally acts as a capacitor in continuous sunlight, thus this method can both discharge capacitive buildup on the SHREWs surface and expel dust from vital connective components (Sims et al., 2003).

5.6.2 Advanced Materials

Frame: The primary consideration in selecting materials for the lunar rover is mass reduction without compromising strength and performance. Teklam honeycomb panels (Collin's Aerospace, 2020) are chosen for the front and rear axle frames as they provide the needed strength for a lunar mission. The commercial variant of this material features a lightweight honeycomb Nomex core, laminated between two thin fiberglass sheets. These Teklam sheets can be folded into three dimensional structures using CNC machines, ovens, and custom tooling. We show that Teklam hollow box-sections offer viable strength for the rover frame through testing described in Section 6.4 and in detail in Appendix G. To account for lunar conditions, a custom Teklam-like material requires an epoxy with a wide working temperature range and that meets NASA outgassing qualification standards. The Supreme 10HT one-component epoxy manufactured by Masterbond meets these specifications with low outgassing and a temperature range of -270°C to 200°C (Masterbond, 2020).

Mid-Frame and Linking Arm: Structural strength is the critical design factor for the mid-frame and linking arm operating in a lunar environment and for surviving mission scenarios. In our terrestrial design, the mid-frame accounts for roughly a quarter of the mass. However, a carbon fiber frame housing the steel lead screw meets mass specifications for the mid-frame while retaining the strength and rigidity of our original concept. The terrestrial linking mechanism is comprised of OEM components for the arm combined with custom aluminum and plastic components for the end effector. We select carbon-fiber and aluminum as the materials for arm, the mechanism, and envelope for the lunar concept. Appendix D shows strength and mass analysis for these components.

Motor Lubricants: Lunar temperature swings require a motor lubricant that can function between extreme temperatures, typically semi solid liquid lubricants and are made up of a combination of oil (liquid) and thickeners (solid). Perfluoropolyethers (PFPE) have widely been used as liquid lubricant in space applications and polymers such as polytetrafluoroethylene (PTFE) are common solid lubricants in space systems. A commercial space-grade lubricant NYETORR 6350EL manufactured by Nye Lubricants is a chemical combination of PFPE/PTFE. The company manufactures many aerospace lubricants, some of which have been used on the ISS and the Mars Curiosity Rover. NYETORR 6350EL has a temperature range of -80°C to 250°C. Though this temperature range does not quite span the lunar surface's temperature range, it has a much larger range than most other lubricants and has low volatility and outgassing factors (NYE Lubricants, 2020). To lubricate the motors and systems of our lunar rover, we would be looking to use a similar PFPE/PTFE grease that has a temperature range that spans the -272°C to 120°C of the lunar surface.

5.6.3. Lunar Electronics

Given the challenges presented by operating in a lunar environment, we do not expect to use off-the-shelf electronic components for the lunar SHREW. Custom, radiation-hardened motor controllers and batteries will minimize packaging mass while meeting demands of space environments. In designing custom components, mass savings emerges by taking advantage of customized design. For example, the terrestrial prototype used three OEM motor controllers, each with two channels, thus reproducing the packaging mass three times over, and including an unused channel. By designing a single motor controller with five channels, we estimate a reduction in mass of these motor controllers by 50% solely through elimination of packaging and reducing wire lengths accordingly.

5.6.4. Thermal Model

To ensure that the sensitive electronics remain within an operating temperature range of -40°C to 60°C they will be enclosed in a WEB that will use a passive paraffin wax heat sink to store and dissipate heat during the mission. Paraffin wax ($\text{C}_{14}\text{H}_{30}$) was selected as the passive heat sink inside the WEB due to its high specific heat capacity as both a liquid and a solid, high heat of fusion, and low melting point (Choi, 2013). The WEB will be double walled to shield the sensitive electronics from solar radiation during the lunar day and to limit the amount of heat radiated away during the lunar night.

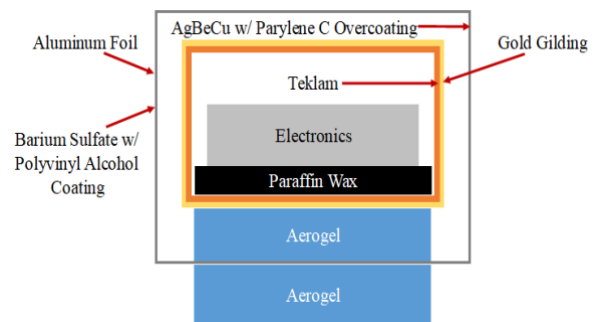


Figure 18: Passive thermal control of WEB.

Figure 18 shows the design concept. The outer box is made of a Teklam core with thermal coatings on its inner and outer surfaces. The outer coating is Barium Sulphate with Polyvinyl Alcohol due to its high emissivity and low absorptance (Henninger, 1984). The inner coating AgBeCu with Parylene C overcoating provides a slightly higher emissivity than absorptance (Henninger, 1984). The inner box serves to limit the amount of thermal radiation emitted during the night. The inner box is made of a Teklam core structure coated in vapor deposited Titanium (Henninger, 1984). The inner titanium coated box contains the electronics, which sit on top of the paraffin wax passive heat sink that stores heat during the day and acts as a heat source at night or inside the PSR. The inner and outer boxes, and the outer box and the rover frame, are separated by layers of aerogel to minimize the heat exchanged between the two boxes and the rover frame via conduction. This is essential as the two boxes and the rover frame will be at different temperature extremes.

A simulation model is developed to size the materials and verify that the electronics inside the WEB can survive the lunar night, lunar day, and that it can remain thermally stable over many lunar days and nights. The simulation uses the material properties and geometries of the different components of the WEB to calculate the heat transfer in the system. Assuming that before the onset of lunar nighttime that the WEB is at its maximum allowable temperature the simulation concludes that the WEB would keep the electronics above the minimum operating temperature of -40°C by using 1.0 kg of paraffin wax and 27 grams of aerogel.

The simulation output for the lunar day indicates that the steady state temperature for the internal electrical components is below the maximum operating temperature of 60°C as shown in Figure 19. The rate at which the WEB increases in temperature is important as it indicates that the WEB will be able to absorb enough solar energy to survive the lunar night in just over 4 days, limiting the amount of time taken away from the mission to harvest thermal energy from the sun. When simulating four lunar days and nights

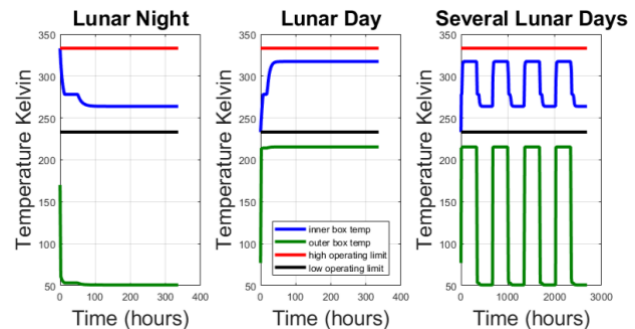


Figure 19: Simulated thermal cycle of passive heat

The simulation output for the lunar day indicates that the steady state temperature for the internal electrical components is below the maximum operating temperature of 60°C as shown in Figure 19. The rate at which the WEB increases in temperature is important as it indicates that the WEB will be able to absorb enough solar energy to survive the lunar night in just over 4 days, limiting the amount of time taken away from the mission to harvest thermal energy from the sun. When simulating four lunar days and nights

we determined that the WEB would stably cycle within the allowable temperature limits over time, rather than trending upwards or downwards in temperature. This is due to the fact that during the lunar day the WEB reaches a steady state maximum temperature ensuring that the starting temperature for each lunar night is the same. These simulations indicate that the WEB will be able to store enough heat to survive the frigid lunar nights and dissipate enough thermal energy to keep the electronics cool during the lunar days.

5.6.5. Teleoperation and Autonomy

A single SHREW entering a PSR would quickly lose line of site and radio contact with the CLPS lander. Since our concept calls for a distributed train of SHREWs to act as signal relays, we can rely on relatively high data rates within the PSR. Based on challenge payload constraints, the mission concept is limited to 1050 kbps per SHREW (70 kbps/kg allowed bandwidth). This data rate is orders of magnitude higher than what is possible between existing Martian rovers and earth, and with a light speed delay of only 1.3 seconds. This data rate for four SHREWs falls within the range required for compressed 720p or 1080p HD video transmission, so some level of continuous video (or equivalent data stream) for teleoperation is possible. A slow-moving rover could also be teleoperated with very low frame rate video, which would allow each of those frames to be of much higher resolution. The Soviet Lunokhod vehicles give us a historical example of such a control scheme, but with a much heavier vehicle (Malenkov, 2016). Lunokhod-1 traveled at 0.28 to 0.56 m/s, which informed and therefore closely matches the speeds proposed here. Operators were able to drive up to 8.3 m at a time, before needing to stop and reevaluate. While Lunokhod could rely on natural light, there is no such luxury in the PSRs. Instead, 3D lidar can be used to produce a directly human viewable image of the environment.

The complex environment within a PSR provides many situations that could lead to temporary or prolonged loss of video connectivity or signal. Therefore, vehicle autonomy must focus on these moments of communication loss. Other than temporary signal losses, most losses will be due to signal attenuation from the environment, with boulders and sharp changes in terrain being the most likely culprits. Therefore, the ability to backtrack the rover's path is critical to reestablishing communication. Autonomy for the SHREWs is as follows: a human operator viewing a continuous data feed from the vehicle can cross reference it against satellite or other remote sensing data to select a path. While this path starts out as an approximation of the intended route, it is made more specific based on data from the rover, eventually specifying the vehicles' intended path down to 10-cm level accuracy. This path is sent to the rover and executed by onboard path following algorithms that sets individual wheel speeds, joint angles, etc. as needed. If the vehicle experiences a loss of signal that it determines requires action (as opposed to simply waiting), it will retrace its steps and returns along the same path. The vehicle relies on simultaneous localization and mapping (SLAM) to navigate when no human operator can act as a guide. Allan et al. (2019) created a lunar analog simulation environment within the existing Gazebo software to help train image-based navigation algorithms, and such a system could also be used to train and test lidar based algorithms before hardware testing.

5.6.6. Comparison to Terrestrial Prototype

Table 3 provides a summary of expected lunar design specifications and lunar mass relative to the terrestrial prototype while using advanced materials, custom electronics, and meeting thermal requirements. In addition to mass reduction through the use of advanced materials, certain components are lighter than their terrestrial counterpart owing to the lower gravitational force on the moon and the lower mass vehicle. For example, the lunar motor-gearheads are a size smaller with two-stage gearboxes, and the narrower wheels achieve the same low ground pressure as the terrestrial vehicle. Mass estimates in Table 3 reflect these design modifications.

Table 3: Comparison of Technical Specifications between Earth and Moon vehicles				
Parameter	Lunar Vehicle		Proof of Concept Vehicle	
<u>Bill of Materials</u>	<u>Material</u>	<u>Mass</u>	<u>Material</u>	<u>Mass</u>
Frame	Teklam Honeycomb Panel	0.63 kg	Aluminum	1.36 kg
Wheels	Aluminum	1.61 kg	Aluminum with plastic inserts	3.41 kg
Winch	Aluminum with Kevlar cable	2.75 kg	Aluminum with Dyneema cable	2.83 kg
Mid-Frame	Carbon fiber and steel	3.51 kg	Aluminum and steel	4.35 kg
Linking Arm and Envelope	Carbon fiber and aluminum	1.65 kg	Aluminum, steel and copper	2.65 kg
Dust Cover	Teflon T-164/Beta 4484	0.17 kg	Cotton Canvas	0.15 kg
Motors/Drivetrain	N/a	1.16 kg	N/a	3.74 kg
Electronics Box	Teklam with passive thermal elements	3.85 kg	Plywood	3.14 kg
Nominal Mass Total		12.6 kg		18.9 kg
Total w/ Winch & Arm		15.3 kg		21.6 kg
Total w/ Payload	Micro-GPR Spectrometer	13.5 kg or 15.5	Simulated Payload	22.6 kg
<u>Payload</u>	Micro GPR System (< 1 kg) Spectrometer (< 3 kg)		Mass Simulator	
<u>Power</u>	Minimum 500 Wh		576 Wh	
Energy Capacity	15 km		17 km	
Operating distance	20 hours driving / 57 hours passive		11 hours driving / 93 hours passive	
Max Operating time	28V DC (provided by the lander)		24-32V DC	
Operating voltage				
<u>Motor Specs</u>	Brushless DC with custom 2-Stage Gearbox, gr 33.22:1		Brushless DC with OEM 3-Stage Gearbox, gr 63:1	
Drive Motors	0.8 Nm		6 Nm	
Max Continuous Torque				
<u>Volume</u>	0.192 m ³		0.213 m ³	
Transport Configuration	0.298 m ³		0.331 m ³	
Driving Configuration				
<u>Thermal System</u>	-40°C to 60°C		N/a	
Electronics Operating Range				

6. Proof-of-Concept Testing on Earth

Two prototype vehicles were constructed in order to begin verification of the terrestrial design and simulations presented in Section 5. All physical testing was conducted locally owing to COVID-19 restrictions on student and employee travel outside of the Hanover, NH region.

6.1. Locomotion Testing

We conducted testing of a single SHREW on flat grass-covered ground, grass-covered slopes, and sand-covered terrain. This testing assessed the performance of wheel speed controllers combined with yaw angle control to enable the vehicle to drive as a rigid body, and assessed steering, hill climbing, and its ability to traverse friable terrain, specifically sand. For straight-line motion, the rover can consistently maintain a straight-line heading within 1° per 10 meters on grass. Asymmetric steering, with front and rear motor frames turned by different amounts; symmetric steering, with both motor frames turned by equal amounts in opposite directions; and crab movement driving, in which wheel axes were parallel but the mid-frame was not perpendicular to the axles, all behaved as intended. Turning configurations in which yaw angles are controlled relative to the mid-frame, along with wheel speed control, prevents scrubbing that can damage wheels. The minimum turn radius is 0.75 m, and a SHREW can climb a grassy slope of up to 25° with limited mobility on heavily vegetated slopes of 30°. Figure 20 shows sequences of video frames from testing symmetric steering and hill climbing. Testing performed in sand with and without wheel inserts confirmed lower sinkage with inserts (3 cm) than without (4 to 7.5 cm), verifying compliance with ground

pressure requirements. Using inserts reduces immobilization events on sand. With inserts, the SHREW can traverse sand mounds of at least 25.5 cm (Figure 21).

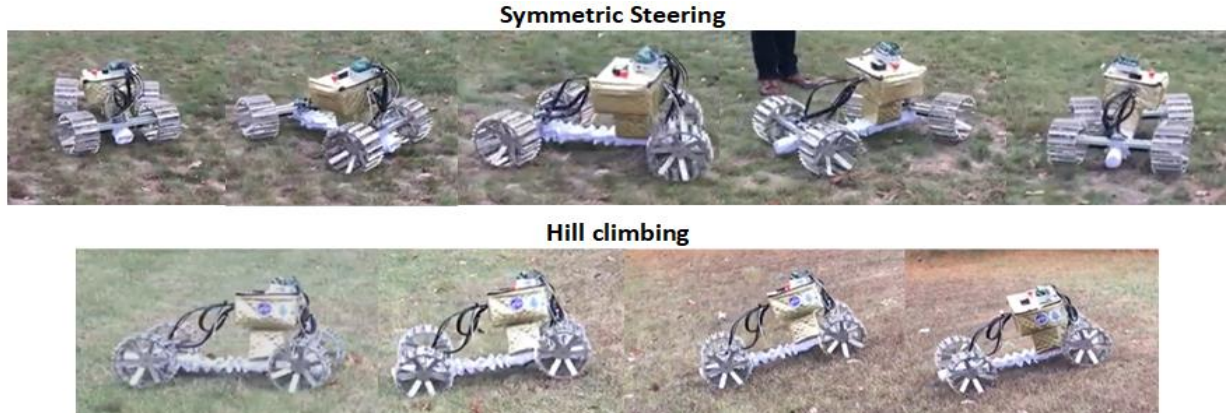


Figure 20: Sequences of a SHREW completing a turn controlled symmetrically (Top) & climbing a grass hill (Bottom).

Sand testing showed that limited ground clearance (8 cm) for the mid-frame must be resolved in a subsequent design iteration. When the SHREW approaches sand obstacles greater than this height head-on, the vehicle can become high-centered and immobilized unless it can “plow” through the soft terrain. For rigid obstacles, the lack of clearance limits forward motion entirely, necessitating alternative maneuvers. The next iteration of the SHREW design could place the mid-frame above the motor frames with a shallower WEB, inverting the placement of components.



Figure 21: Snapshots of a SHREW operating in sand with and without wheel inserts.

Benchtop testing verified the actuation of the mid-frame joint through manual commands to expand/contract the wheelbase. Figure 22 shows a full actuation sequence from the maximum wheelbase to the minimum allowable wheelbase. These tests showed that this concept can be incorporated into locomotion modes. These tests also show that on the prototype vehicle, the motor used for actuating the frame needs an alternate gearbox to provide higher torque and lower speed, as we used an existing motor in order to preserve budget funds needed to build two robots.



Figure 22: Sequence showing actuation of the mid-frame.

6.2. Linking Tests

Tests conducted with the linking arm verify that two SHREWs can mechanically and electrically join when positioned at different distances, angles and heights. Throughout these tests, small adjustments were made to the linking algorithm to ensure that it was possible to mechanically mate in the full range of positions. We verified that the SHREWs could autonomously connect when they were within 50-80 cm of each other, facing each other within ± 45 degrees, and had a height difference under 30 cm. Furthermore, we tested the linking of SHREWs in total darkness, with the arm tracking a 100 lumen LED rather than the colored disk. Figure 23 shows a snapshot from this test.

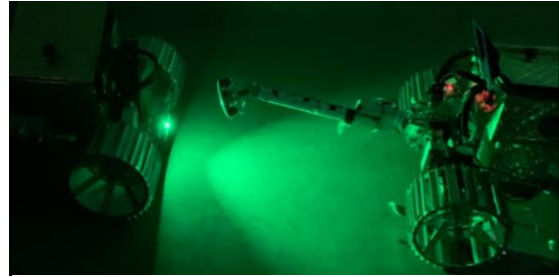


Figure 23: Linking test in darkness.

In addition to testing the SHREWs' ability to mate mechanically, we also verified that the two vehicles could connect electrically to transfer power. This was done by adding a 12V circuit with a buzzer to the linking envelope busbars and connecting the power and ground busbars on the end effector plug. When the arm successfully connects the two SHREWs, the buzzer sounds, demonstrating that the busbars on the plug and envelope are in contact and the circuit closed.

While the range of alignment positions and overall consistency of the arm could be improved with adjustments to the software and mechanical design, the results of these tests demonstrate that this technology is viable and can be adapted to work in a lunar environment with imperfect positioning.

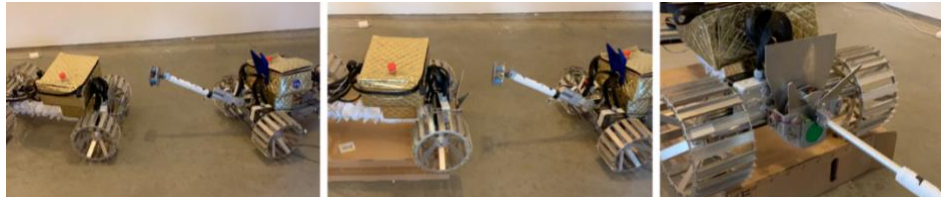


Figure 24: Linking of vehicle units at variable heights and angles.

6.3. Testing of Teklam Frame Elements

To validate the potential for using Nomex honeycomb sheets for the lunar vehicle frame, we constructed a box-section frame from 0.25" Nomex sheet with fiberglass facings. Flexural testing of beam sections under 3-point mid span loading, 4-point third span loading, and 4-point quarter span



Figure 25: Flexural Testing of Teklam frame

loading using an Instron 4469 with a 50kN load cell provided the results shown in Table 4. Testing was conducted to ASTM standard C393 and C393M, modified to the properties of our beam (Figure 25).

Table 4. Results of Instron testing of a structural member fabricated from Nomex			
Condition	Yield Force (kN)	Average Bending Rigidity (N/m)	Average Elastic Modulus (MPa/m)
3-point loading	1.63	4589	.79
4-point quarter span loading	2.74	6467	1.11
4-point third span loading	3.58	6455	1.11

Standard D7250/D7250M was used to determine the flexural and shear stiffness of the members. Force was applied vertically through the loading bars with the support bars beneath it fixed. Small buffer blocks were placed over the support and loading rollers to limit the impact of flatwise compression, which crushes the interior Nomex prior to reaching the yielding strength. Testing determined that employment of such materials will undoubtedly provide sufficient strength to resist even the most severe bending conditions the vehicle may encounter during its mission.

6.4. Energy Consumption

The terrestrial prototype's as-tested mass is 21.4 kg and energy consumption was measured during a 400 ± 10 m endurance test as 30 km/kWh while traversing a flat grassy surface at 0.42 m/s. This is based on the total power consumption of the vehicle including the low voltage electronics, which draw 5 to 8 W. On sand (used as our lunar soil analog), instantaneous power was measured while driving straight at 0.46 m/s along a 6.5 m track as 63.7 to 68.8 W. Excluding the housekeeping power of 5 to 8 W results in a projected endurance of 27 km/kWh of energy to the wheels. Using an estimated terrain resistance of 0.3, the calculated endurance is 50 km/kWh, which means the as-fabricated drivetrain has an efficiency of 54% compared to the ideal case, the terrain resistance is higher than 0.3, or some combination of these two factors.

Under the mission scenario identified in section 5.1, the SHREW that explores the crater consumes the largest energy of the four rovers. We assume baseline or housekeeping power of 13 W for radiation-hardened electronics, 8 W average drive power, and 3W of power for scientific instruments. Scaling the terrestrial vehicle's drive energy of 27 km/kWh to the lunar condition and adding expected housekeeping power and instrument power provides the required 20 hours of operation with a 500 Wh battery. Detailed calculations for the energy consumption can be found in Appendix H.

6.5. Critical Testing not Performed

The COVID-19 pandemic led to the closure of university facilities and research labs from mid-March to early June 2020. This led to the entirety of mission development, simulation work, and detailed design of physical prototypes being completed asynchronously and virtually. Laboratory access remained closed to undergraduates throughout the remainder of the project. Our team was forced to abandon our plan to visit and/or perform testing at the GRC SLOPE Lab. The remote work environment complicated the team's ability to rapidly troubleshoot problems that appeared while integrating components into a rover system.

Physical testing remaining includes embedded control and testing of push-pull locomotion on sand for individual SHREWs and push-pull locomotion on soft terrain for the two linked vehicles. Quantification of mobility characteristics should include drawbar pull tests on GRC-1 lunar soil strength simulant on both flat surfaces and on the adjustable tilt-bed in the NASA SLOPE Lab. One metric of success for these tests is whether a SHREW robot can match or surpass the 40% added pull-force presently met by the Scarab Rover (Creager 2012). Further testing also remains for winching on an incline attached to the winch. These tests should quantify max slope gradient as well as required motor motion to ensure a static pulling/lowering robot.

7. Test Results & Conclusions

SHREWs accomplish goal three of the NASA Big Idea 2020 Challenge – providing capabilities to explore and operate in PSRs. Specifically, they provide innovations in mobility systems, providing a method for a caravan of robots to traverse previously impassable terrain, and conduct prolonged missions in PSRs utilizing solar power. Extensive design, validation, and testing have resulted in a concept science platform that enables long term exploration of PSRs in hazardous terrain. The combination of Gazebo/ROS simulation and terrestrial prototype testing confirmed that the SHREW concept is able to operate in friable

terrain with the aid of the expanding and contracting mid-joint and is expected to achieve the proposed mission plan through the caravan concept. The mid-joint concept provides locomotion modes that reduce risk of immobilization. Shackleton Crater exhibits a maximum gradient of 35° , and testing showed excessive slip at $30\text{-}35^\circ$ on wet leaves, but positive traction at over $15\text{-}20^\circ$, while the winch generates sufficient force to pull a robot up the 35° slope. The SHREWs are expected to be able to traverse basin terrain and navigate up and down the crater walls to accomplish mission directives. The connector arm conducts electrical energy across the arm connection, enabling power transmission and recharge of individual SHREWs.

8. Safety Plan and Protocols Followed

Project development followed best practices regarding emergency escape plans, safety and training, and equipment specified by our institution. Broadly, these can be found here: <https://engineering.dartmouth.edu/people/offices/facilities-planning-operations>. As it pertains to the COVID-19 pandemic, the team complied with guidelines set by Dartmouth College and the state of New Hampshire. Travel for all team members was limited to a 20-mile radius from the college, and proper quarantining and social distancing was practiced where this restriction could not be maintained. All work done in person by multiple team members included the wearing of masks and maintaining 6-feet between group members.

9. Path-To-Flight

Our rover concept is on track to be deployed to the lunar surface prior to human arrival on Artemis III in 2023. Our team intends to pursue Phase B funding in the early spring of 2021. A nine-month refinement period will take place in which technical specificity is increased, specifically in collaboration with GRC for wheel designs and real-environment testing. Subsequently, the project will be passed over to STMD for management. JPL and JSC will collaborate to make a lunar prototype to the requirements found here and in Phase B activities. By mid-2023, the project will near deployment to the lunar surface and STMD will transition management to SMD.

At the time of our proposal, the SHREW concept was consistent with TRL 2, defined as “Technology concept and/or application formulated... Invention begins, practical applications identified but speculative, no experimental proof or detailed analysis is available to support the conjecture.” Over the performance period (mid-February 2020 to late Nov 2020), we have taken SHREW system and subsystem concepts from TRL 2 to TRL 3 to 4, identified as follows based on NASA TRL definitions provided in NASA (2020f). **SHREW Concept:** The 9 DOF 4WD vehicle with independent front and rear axle roll/yaw DOFs and mid-frame joint is consistent with **TRL 4:** “A low fidelity system...is built and operated to demonstrate basic functionality and critical test environments, and associated performance predictions are defined relative to final operating environment. Key, functionality critical software components are integrated and functionally validated to...begin architecture development. Relevant environments defined and performance in the environment predicted.” Justification: The SHREW earth-analog prototype with key control software demonstrated independent control of yaw DOFs in “lab” environment (on grass and sand-covered terrain), and power/energy consumption is documented. **Midframe joint subsystem:** Mid-frame joint for augmented trafficability of terrain for single SHREW is consistent with **TRL 3:** “Analytical studies place the technology in an appropriate context and laboratory demonstrations, modeling and simulation validate analytical prediction. Development of limited functionality to validate critical properties and predictions ...”. Justification: mid-frame joint prototype designed, implemented, and bench tested. Simulation model and control of “inchworm” behavior is demonstrated in Gazebo with simple state machine triggering the inchworm mode. Benefits to mobility in soft terrain demonstrated. **SHREW Caravan concept:** Linking of individual SHREWs for mission-specific tasks is consistent with **TRL 3.** Justification: The V-envelope and connection arm are prototyped and software functionality/joining using image processing demonstrated. A simulation model of caravan control modes is implemented in Gazebo. Benefits to mobility are demonstrated. **SHREW Winch subsystem:** The winch is consistent with TRL 3.

Justification: Functionality of the terrestrial prototype in winding, unwinding, and delivering required torque is tested in a laboratory setting.

10. Detailed Timeline

Sept. 26, 2019	Submission of Notice of Intent to apply to challenge; early concept design and problem assessment by Adam Gronewold and Laura Ray.
Nov. 15, 2019	First CAD design of conceptual design completed.
Jan. 5, 2020	Austin Lines added to team to lead terramechanics and help lead concept and detailed design. Joshua Elliott added to team to lead circuit design and ROS simulation. Grace Player and Marguerite Genereux added to team to assist in mechanical design and to lead verification of concept for lunar environment. Chris Lyke added to team for mechanical design, verification of linking mechanism.
Jan. 16, 2020	Submission to 2020 NASA BIG Idea Challenge.
Feb. 14, 2020	Team notified of selection to the Challenge.
Feb. 15-25, 2020	Reassessment in order to assemble the requested two prototype vehicles within budget constraints, despite proposing the construction of one prototype vehicle.
Feb. 21 – March 1, 2020	Testing on lunar vehicle frame constructed from a box section beam, constructed from Nomex core honeycomb sandwich sheet with fiberglass facings. 3-point, 4-point bending to ASTM standard C297. Found that such beams are structurally sufficient to meet loading conditions on the moon and through both launch and descent.
March 1 – April 16, 2020	Mission scenario assessment and concept modification. Selection of potential crater sites using LOLA data and JPL's Moon Trek.
March 1 – May 1, 2020	Further conceptual modification of internal joint mid-frame, winch, and linking mechanism based on mission scenario.
March 17, 2020	Dartmouth announces COVID-19 closures for spring term. Thayer School of Engineering laboratory research officially shutdowns. Team moved to remote work across the country.
April 4, 2020	Andrew Skow added to team to lead thermal simulation, to assist in concept iteration and assembly.
April 10 – May 10, 2020	Simulation of thermal model and thermal cycle for paraffin wax heat exchanger on lunar environment.
May 12, 2020	Mid-project report submitted. 1 st version of detailed design. Linking mechanism, winch and internal joint needing further iteration.
May 24, 2020	Finalized design of wheels following simulation of von Mises stresses and strain
May 27, 2020	Notified of pass status for second installment of funding. Concerns relayed by judges expedite part ordering and mechanical assembly.
May 25 – June 1, 2020	Final design review completion and solidification of prototype design. CAD model completed of full vehicle. Finalized Bill of Materials.
June 2, 2020	Motors and motor controllers ordered (anticipated lead times of two weeks).
June 4 – 15, 2020	Majority of part purchasing. Engineering drawings made for custom parts for manufacture, submitted incrementally to Thayer Machine Shop.
June 15, 2020	First garage labs set up in Illinois and Wisconsin for individual team members to assemble parts when received.
June 20, 2020	Motor controllers received. We also learned the company sourcing our motors failed to finalize our purchase, thus setting back the lead time on the motors until mid-July.
July 2, 2020	Wheel parts received and linking mechanism parts received.
July 5, 2020	Wheel assembly completed. Initial testing of positioning and calibration of camera system for connector arm.
July 8 - 15, 2020	Majority of mechanical parts (waiting on motors) and half electronics parts received for assembly in Illinois.
July 28, 2020	Motors finally received, 5 weeks after anticipated.
Aug. 8, 2020	Full mechanical assembly completed, with exception to the electronics box.
Aug. 9, 2020	Second series of tests completed on linking mechanism tracking system. High level of consistency achieved with a first version prototype circuit and code. Manual calibration GUI fully implemented.
Aug. 9 – 17, 2020	Electronics boxes made by hand. Dust covers hand sewn.
Aug. 21, 2020	Project moved from garages in Illinois and Wisconsin to second garage laboratory at team lead's apartment in New Hampshire for the completion of circuit wiring by multiple team members, with social distancing and mask wearing. Dartmouth travel restrictions remain in place limiting testing at external facilities.

Aug. 26 – Sept. 24, 2020	Initial wiring seems completed. Motor controllers do not boot as designed using relay circuits to power the robot on and off. Significant troubleshooting and sub-circuit isolation. Problem is a consequence of faulty DC-DC converter or odd level shifting caused by the use of relays.
Sept. 14, 2020	Phillip Mulford added to the team to lead testing on winch and assist in code implementation.
Sept. 20, 2020	Advanced implementation of control and simulation in ROS and Gazebo.
Sept. 26, 2020	Garage lab moves again due to space constraints in former space, following approval from Dean of Thayer School. Although College's labs were then open for graduate students, undergraduates still restricted from formal, non-garage lab spaces.
Sept. 27 – Oct. 11, 2020	We learn 4 of 6 motor controllers purchased were dead-on-arrival after extensive troubleshooting. Products replaced in one week. Completed rewiring of motor controller circuits to be powered on with manual switches, as relays failed to work despite recommendations from controller company. DC-DC converters removed from circuit.
Oct. 3, 2020	Managed to set up one of two working controllers. First commands, sent open-loop via controller PC utility, realized by motors. Began implementing control laws where possible, while we waited for other motor controllers.
Oct. 7, 2020	Canvas dust cover sewn for internal joint.
Oct. 12, 2020	First commands sent to all four wheels, closed-loop speed control, from robot's on-board computer. Control gains tuned for settling time under 2 seconds.
Oct. 14, 2020	Finished adding copper busbars to connector arm end effector and our linking envelope. Tested electrical connection for the first time, showing the circuit can be closed manually.
Oct. 26, 2020	Successfully had arm find and connect to the linking envelope in controlled environment detached from vehicle.
Oct. 31, 2020	Implemented outer control loop to maintain set reference angles on both yaw joints. Successful first tests on grass with straight line operation, symmetric steer without skid, and asymmetric steer with skid, without incident. Robot successfully traversed 20 degree slope in grass. Identified limitation on 25 degree slope.
Nov. 5, 2020	Purchased 2500 lbs. of fine grain sand for further testing in more accurate environment.
Nov. 4-9, 2020	Further simulation of vehicle control under lunar gravity in custom Gazebo environment.
Nov. 13, 2020	First tests in sand. Identified failure mode where wheels dig in on noncohesive soils ~56% of wheel diameter, without added control from internal joint. Due to slots in grousers.
Nov. 15, 2020	Linking mechanisms fully attached to SHREW. LED added to prepare for testing of the connection in the dark and buzzers to indicate electrical connection established.
Nov. 18, 2020	Successful tests of arm performing linking maneuver between two SHREWs, establishing electrical connection from various pitch and yaw angles.
Nov. 20, 2020	Plastic backing added to rover wheels to close slots between grousers in order to limit sand flowing into the wheel and causing the vehicle to become high centered.
Nov. 20, 2020	Testing of linking in low light with tracking of LED. Vehicle can effectively perform such attachment and establish electrical connection semiautonomously.
Nov. 22, 2020	Power testing; testing of plastic wheel inserts, limit testing of trafficable bumps in noncohesive soil.
Nov 25, 2020	Mid-frame actuation tests: Demonstrated baseline functionality of expanding frame.

11. Detailed Budget

Table 5 shows actual and encumbered expenditures for each budget period. Note that funds for budget period 2 were delayed and not received until early November due to paperwork needed to transmit funds through the New Hampshire Space Grant. For this reason, we performed an internal transfer moving expenditures from Budget Period 1 to Period 2, because Period 2 must be spent prior to Period 1 funds. Encumbered funds are costs incurred between Nov 29 and Jan 6 and expenses expected to be incurred subsequent to the final presentations. We expect to work on the project beyond the competition presentation in order to achieve additional objectives that were not possible due to COVID-19 travel constraints. Residual funds will be used for materials to resize the internal joint motors, for graduate support to continue implementing control code for mobility mode switching, and for testing in terrain not available in the immediate vicinity. Travel funds initially planned to attend the onsite BIG Idea event are reallocated for graduate student support. Remaining budget categories remain largely unchanged from the original proposal. In addition to the \$83,000 NASA award, other sources of support include Thayer School fellowships to graduate students, a Clare Booth Luce research fellowship to Grace Player, and cost shared indirect costs totaling \$101,000.

Table 5: Summary of Exdatures under SHREW Development			
Category	Budget period 1	Budget period 2	Total
Fabricated equipment			
Expense	\$ -	\$ 21,956.84	\$ 21,956.84
Encumbered	\$ 1,900.00	\$ 900.00	\$ 2,800.00
Total fabricated equipment	\$ 1,900.00	\$ 22,856.84	\$ 24,756.84
Payroll			
Faculty encumbered	\$ 3,083.00	\$ -	\$ 3,083.00
Graduate student	\$ -	\$ 6,110.50	\$ 6,110.50
Graduate student encumbered	\$ 25,894.66	\$ 7,328.00	\$ 33,222.66
Undergraduate stipend expense	\$ 288.75	\$ 4,543.32	\$ 4,832.07
Undergraduate stipend encumbered	\$ 767.93	\$ -	\$ 767.93
Total payroll	\$ 30,034.34	\$ 17,981.82	\$ 48,016.16
Purchased service			
Expense	\$ -	\$ -	\$ -
Encumbered	\$ 900.00	\$ -	\$ 900.00
Total purchased services	\$ 900.00	\$ -	\$ 900.00
Supplies			
Expense	\$ -	\$ -	\$ -
Encumbered	\$ 600.00	\$ -	\$ 600.00
Total Supplies	\$ 600.00	\$ -	\$ 600.00
Total direct costs	\$ 33,434.34	\$ 40,838.66	\$ 74,273.00
Indirect costs (actual and encumbered)	\$ 4,631.39	\$ 4,095.61	\$ 8,727.00
Total (direct + indirect)	\$ 38,065.73	\$ 44,934.27	\$ 83,000.00
Other sources of support			
Thayer School Graduate Fellowships (supports Philip Mulford)			\$ 29,613.67
Clare Booth Luce research fellowship (Grace Player)			\$ 3,000.00
Partial indirect cost share			\$ 38,807.71
Thayer School Ph.D. Innovation Fellowship (supports Joshua Elliot)			\$ 29,613.67
Total (other sources)			\$ 101,035.05

Appendix A: References

Allan, M., Wong, U., Furlong, P. M., Rogg, A., McMichael, S., Welsh, T., Chen, I., Peters, S., Gerkey, B., Quigley, M., Deans, M., Cannon, H., Fong, T & Shirley, M. (2019). Planetary rover simulation for lunar exploration missions. In *2019 IEEE Aerospace Conference. IEEE*. (pp. 1-19).

Arcone, S. (2020). Thayer School Adjunct Professor and GPR expert, personal communication.

Bandyopadhyay, S (2020). Lunar Crater Radio Telescope (LCRT) on the Far-Side of the Moon. *NASA Press Release*. https://www.nasa.gov/directorates/spacetech/niac/2020_Phase_I_Phase_II/lunar_crater_radio_telescope/.

Bron Aerotech. (2020). *BA 500BC/CF500F (Beta Cloth, Beta Fabric)*. <https://bronaerotech.com/product/ba-500bc-cf500f-beta-cloth/>.

Carrier, W. David. (1996). Trafficability of Lunar Microrovers (Part 3) (LGI TR96-01). *Lunar Geotechnical Institute*. https://www.lpi.usra.edu/lunar/surface/Trafficability_Part_3.pdf.

Choi, Michael K. (2013). Using Paraffin with -10 deg C to 10 deg C Melting Point for Payload Thermal Energy Storage in SpaceX Dragon Trunk. *NASA Goddard Space Flight Center*. <https://ntrs.nasa.gov/api/citations/20160000793/downloads/20160000793.pdf>.

Christofferson, R., Lindsay, J. F., Noble, S. K., Meador, Mary Ann, Kosmo, J. J., Lawrence, J. A., Brostoff, L., Young, A. & McCue, T. (2009). Lunar dust effects on spacesuit systems. *Johnson Space Center*. <https://www.si.edu/content/MCIImagingStudio/papers/Lunar%20Dust%20Effects%20Spacesuit%20System.ms.pdf>.

Clark, R. N. (2009). Detection of Adsorbed Water and Hydroxyl on the Moon. *Science*, 326(5952), 562– 564. <https://doi.org/DOI: 10.1126/science.1178105>. <https://science.sciencemag.org/content/326/5952/562>.

Collin's Aerospace (2020). *Honeycomb Panels*. <https://www.collinsaerospace.com/what-we-do/Commercial-Aviation/Cabin/Structures/Honeycomb-Panels>.

Creager, C., Johnson, K., Plant, M., Moreland, S., & Skonieczny, K. (2014). Push–pull locomotion for vehicle extrication. *Journal of Terramechanics*, 57, 71–80. <https://doi.org/10.1016/j.jterra.2014.12.001>.

Creager, C., Moreland, S., Skonieczny, K., Johnson, K., Asnani, V., & Gilligan, R. (2012). Benefit of "Push-Pull" Locomotion for Planetary Rover Mobility. In *Earth and Space 2012: Engineering, Science, Construction, and Operations in Challenging Environments*. (pp. 11-20).

ElectroCraft, Hansen Corp. (2020). *LRPX40 Brushless DC Planetary Gear Motor*. <https://www.electrocraft.com/products/bldc/LRPX40/>.

Finckenor, M. & Doolin, D. (1999). Multilayer Insulation Material Guidelines. NASA Technical Report NASA/TP—1999–209263. *Marshall Space Flight Center*. <http://www.dept.aoe.vt.edu/~cdhall/courses/aoe4065/NASADesignSPs/tp209263.pdf>.

Gaier, J. R., Journey, K., Christopher, S. & Davis, S. (2011, December). Evaluation of brushing as a lunar dust mitigation strategy for thermal control surfaces. *Glenn Research Center*. <https://ntrs.nasa.gov/api/citations/20120000070/downloads/20120000070.pdf>.

Gurley Precision Instruments (2020). *MIL and Space Encoders*. <https://www.gurley.com/milspace-encoders>.

Henninger, J. H. (1984). Solar absorptance and thermal emittance of some common spacecraft thermal- control coatings. *NASA Goddard Space Flight Center*. <https://ntrs.nasa.gov/api/citations/19840015630/downloads/19840015630.pdf>.

Kim, S. S., Carnes, S. R., Haldemann, A. F., Ng, E. H. W., Ulmer, C. T., & Arcone, S. A. (2006, March). Miniature ground penetrating radar, CRUX GPR. In *2006 IEEE Aerospace Conference. IEEE*. (pp. 7-pp).

Kring, D. & Durda, D., LPI/JSC (2012). A Global Lunar Landing Site Study to Provide the Scientific Context for Exploration of the Moon. *National Research Council*. <https://www.lpi.usra.edu/exploration/CLSE-landing-site-study/>.

- Lucey, P. G., Neumann, G. A., Riner, M. A., Mazarico, E., Smith, D. E., Zuber, M. T., Paige, D. A., Bussey, D. B., Cahill, J. T., McGovern, A., Isaacson, P., Corley, L. M., Torrence, M. H., Melosh, H. J., Head, J. W., & Song, E. (2014). The global albedo of the Moon at 1064 nm from LOLA. *Journal of Geophysical Research: Planets*, 119, 1665–1679. <https://doi.org/10.1002/2013JE004592>.
- Malenkov, M. (2016). Self-propelled automatic chassis of Lunokhod-1: History of creation in episodes. *Frontiers of Mechanical Engineering*, 11(1), (pp. 60-86).
- Masterbond (2020). *Supreme 10HT One component, toughened epoxy system*. <https://www.masterbond.com/tds/supreme-10ht>.
- McGarey, P., W. Reid & Nesnas I. (2019). Towards Articulated Mobility and Efficient Docking for the DuAxel Tethered Robot System. *IEEE Aerospace Conference*, (pp. 1-9). doi: 10.1109/AERO.2019.8741573.
- NASA. (2009). LCROSS Impact Data Indicates Water on Moon. https://www.nasa.gov/mission_pages/LCROSS/main/prelim_water_results.html.
- NASA. (2019, July 16). Spirit: In Depth. *NASA Science: Solar System Exploration*. <https://solarsystem.nasa.gov/missions/spirit/in-depth/>.
- NASA (2020a). 2020 NASA Technology Taxonomy. https://www.nasa.gov/sites/default/files/atoms/files/2020_nasa_technology_taxonomy_lowres.pdf.
- NASA (2020b). NASA Systems Engineering Handbook (SP-6105, Rev. 2). <https://www.nasa.gov/connect/ebooks/nasa-systems-engineering-handbook/>.
- NASA. (2020c). The Artemis Plan (NP-2020-05-2853-HQ). Washington D.C. https://www.nasa.gov/sites/default/files/atoms/files/artemis_plan-20200921.pdf.
- NASA (2020d). Moon Trek. <https://trek.nasa.gov/moon/#v=0.1&x=0&y=0&z=1&p=urn%3Aogc%3Adef%3Acrs%3AEPG%3A%3A104903&d=&locale=&b=moon&e=-165.58593441123168%2C-161.36718448992642%2C165.58593441123168%2C161.36718448992642&sfz=&w=>.
- NASA (2020e). Mars 2020 Perseverance Mission. RIMFAX. <https://mars.nasa.gov/mars2020/spacescraft/instruments/rimfax/>.
- NASA (2020f). NASA TRL Definitions. https://www.nasa.gov/pdf/458490main_TRL_Definitions.pdf.
- Nesnas, I. A., Matthews, J. B., Abad-Manterola, P., Burdick, J. W., Edlund, J. A., Morrison, J. C., Peters, R. D., Tanners, M. M., Miyake, R. N., Solish, B. S., & Anderson, R. C. (2012). Axel and DuAxel rovers for the sustainable exploration of extreme terrains. *Journal of Field Robotics*, 29(4), 663-685.
- Noble, Sarah. (2009, March 17). The lunar regolith. *NASA Marshall Space Flight Center*. <https://ntrs.nasa.gov/api/citations/20090026015/downloads/20090026015.pdf>.
- NYE Lubricants (2020). *NYETORR 6350EL Lubricant*. <https://www.nyelubricants.com/space>.
- R&W Rope (2020). *Amsteel Blue -12 Strand Dyneema Rope*. <https://rwrope.com/products/amsteel-blue-12-strand-dyneema-rope?variant=29561339609141>.
- Sims, R. A., Biris, A. S., Wilson, J. D., Yurteri, C. U., Mazumder, M. K., Calle, C. I. & Buhler, C. R. (2003, January). Development of a transparent self-cleaning dust shield for solar panels. *University of Arkansas at Little Rock & Kennedy Space Center*. <https://physics.ksc.nasa.gov/Publications/Development%20of%20self%20cleaning%20dust%20shield%20-%20RA%20Sims.pdf>
- Smith, D. E., Zuber, M. T., Neumann, G. A., Mazarico, E., Lemoine, F. G., Head, J. W. III, Lucey, P. G., Aharonson, O., Robinson, M. S., Sun, X., Torrence, M. H., Barker, M. K., Oberst, J., Duxbury, T. C., Mao, D.,

Barnouin, O. S., Jha, K., Rowlands, D. D., ... Mcclanahan, T. (2017). Summary of the results from the lunar orbiter laser altimeter after seven years in lunar orbit. *Icarus*, 283, 70–91. <https://doi.org/10.1016/j.icarus.2016.06.006>

Spudis, P. D., Bussey, B., Plescia, J., Josset, J.-L., & Beauvivre, S. (2008). Geology of Shackleton Crater and the south pole of the Moon. *Geophysical Research Letters*, 35(14). <https://doi.org/10.1029/2008gl034468>.

Tabor, A. (2020). When the moon dust settles, it won't settle in VIPER's wheels. *Ames Research Center*. <https://www.nasa.gov/feature/ames/when-the-moon-dust-settles-it-won-t-settle-in-viper-s-wheels>.

Ultralife Corporation (2020). *UBBL13-01 (UBI-2590 10.0Ah High Capacity Smart 2590 Battery with SOCI and SMBus)*. <https://www.ultralifecorporation.com/ECommerce/product/ubi-2590/bb-2590-rechargeable-batteries/ubbl13-01/ubi-2590-high-capacity>.

Wettergreen, D., Jonak, D., Kohanbash, D., Moreland, S., Spiker, S., Teza, J., & Whittaker, W. (2009). Design and Experimentation of a Rover Concept for Lunar Crater Resource Survey. *Carnegie Mellon University, Robotics Institute*.

Appendix B: Wheel Design

For the wheel design and selection of the SHREWs, we scaled down custom aluminum wheels that were developed for a polar rover in Dr. Ray's lab. The wheels were designed to be lightweight, easy to fabricate and maintain, and have effective traction. The wheel's rims and webs are cut from Aluminum 6061 sheets and the webs are bent into shape. The rims, webs and aluminum grousers, pre-cut to length, are then fastened using bolts. From our CAD models, we have determined that this design meets our mass and strength requirements. Using SolidWorks loading simulations, we tested the wheel design under three separate loading conditions:

1. Normal loading:
 - $\frac{1}{4}$ of rover's weight directed down
2. Loading case 2:
 - Rover's entire weight directed down
 - Stall torque of motor being exerted on wheel
3. Worst-case loading: (simulates 75% of robot's weight on one wheel applied at 30° to ground)
 - 73% of robot's weight directed down
 - 42% of robot's weight directed horizontally
 - Stall torque of motor being exerted on wheel

Figure A.1 shows results for normal loading and worst-case loading.

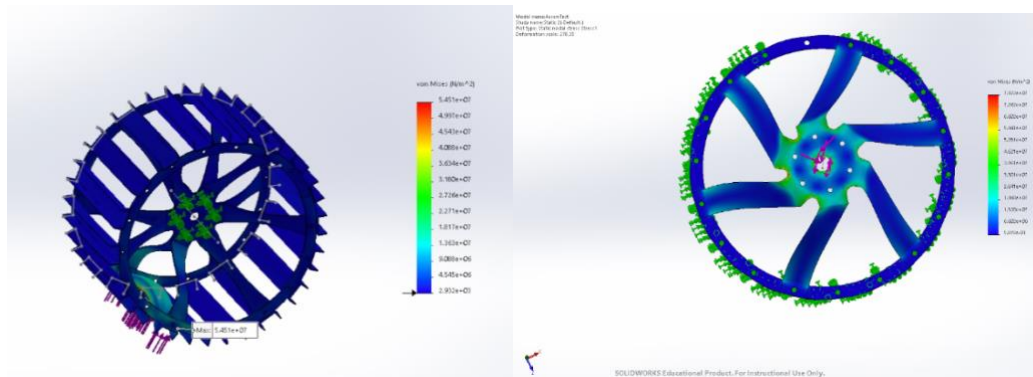


Figure A.1. Earth Rover Wheel Under Normal Loading and Worst-Case Loading.

We tested these loading conditions for varying thicknesses of aluminum for the wheel's rim, spider and grouser, and recorded both the maximum Von-Mises stress and yield strength safety factor from these simulations. Given that Aluminum 6061's yield strength is 276MPa, the yield strength safety factor was calculated by dividing the maximum recorded Von-Mises stress by 276 MPa. Table A.1 shows simulation results.

Table A.1. Simulation Results, Selected Design Highlighted in Yellow.

Rim Thickness	Spider Thickness	Grouser Thickness	Max Von-Mises Stress (MPa)	Yield Strength Safety Factor	Mass per Wheel (g)
0.0907	0.0808	0.045	44.16	4.370471014	748.06
0.0907	0.0808	0.0508	40.22	4.798607658	795.88
0.1019	0.0808	0.045	43.28	4.459334566	762.01
0.0907	0.0907	0.045	44.77	4.310922493	777.16

To accommodate for lunar conditions and mass requirements, the earth rover's wheel design was altered. First, the wheel's diameter was scaled by 90%, which both reduced mass and enabled the use of smaller motors by reducing the required output torque and mechanical power necessary for the rover to travel at a given velocity. The thickness of the aluminum used for the wheel's web and rims were also reduced. To ensure the redesigned wheel's structural strength, the same 3 loading conditions were simulated on SolidWorks using lunar gravity as well as a static loading case using Earth's gravity. From these simulation studies, the maximum von Mises stress recorded on the scaled wheel was of 22.41 MPa, which gives a yield strength safety factor of 8.62.

RO maintain low ground pressure of the lunar rover when redesigning the wheels and save mass, the width of the wheel was reduced to 72.2 mm. Assuming one of each wheels' grousers are in contact with the lunar surface, the lunar rover has a moon ground pressure of 3.69 kPa. With these modifications, each of the lunar rover wheels weighs 0.38 kg, for a total of 1.52 kg for all four wheels of the rover.

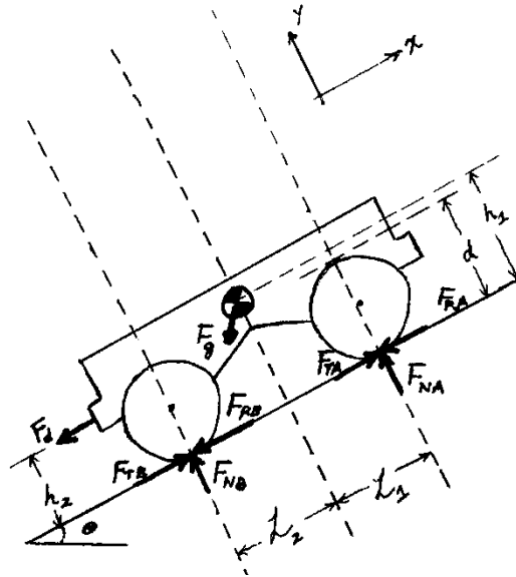
Appendix C: Motor Selection Calculations

Adam Gronewold – March 2020

Equilibrium Equations

For the selection of DC motors and gearheads of SHREWs, we make the following formulation, with a focus on retaining efficiency where possible.

Beginning with a freebody diagram, Figure C.1, of the vehicle progressing up a slope at a desired steady-state velocity, in order to find the steady-state torque required for a given angle. For the selection of DC motors and gearheads of SHREWs, we make the following formulation, with a focus on retaining efficiency.



θ angle of slope	F_{RA} resistance force on front wheels
F_d drawbar pull	F_{RB} resistance force on back wheels
F_{NA} normal force on front wheels	d wheel diameter
F_{NB} normal force on back wheels	h_1 center of mass height
F_g force due to gravity	h_2 drawbar height
F_{TA} tractive force from front wheels	L_1 front to mass center length
F_{TB} tractive force from back wheels	L_2 rear to mass center length
m vehicle mass	a acceleration

Figure C.1: Freebody diagram

I make the following assumptions:

1. From our concept mission scenario, the average slope of craters of interest is greater than 15 degrees. Control of position on the slope will largely be done via winch, with assistance from braking torques from the wheels. So, we size our motors for slopes less than this at, $0^\circ \leq \theta \leq 15^\circ$. This provides will provide the vehicles with enough mechanical power to be mobile on relatively steep slopes without sizing them beyond what is reasonable to expect on friable surfaces like sand or the lunar regolith.
2. We assume $L_1=L_2$. As such, the normal force on the front wheels is numerically equivalent to that of the back wheels, $F_{NA}=F_{NB}$, regardless of slope.
3. $d=h_1=h_2$.
4. Resistance, represented by parameters F_{RA} and F_{RB} , is defined as the collective resistance to constant motion, antiparallel to the direction of the motion. This includes resistance due to

internal friction in bearings, resistance due to changes in shape of the surface (compaction, bulldozing), etc.

5. $F_{RA} = C_{\tau} F_{NA}$ and similarly for point B. Because the regolith is expected to deform substantially beneath the weight of our vehicle, and because the wheel type we select is highly variable, we assume a high coefficient of rolling resistance, C_{τ} , as a safety margin. Likewise, we only consider the normal force as a function of mass and angle.
6. Additionally, this selection is made with the thinking that the regolith is so soft, and thus so plastic, that our wheels are entirely rigid.

From our equilibrium equations, we find then that the tractive trust force required by each wheel is given by:

$$F_T = 0.5 F_{TA} = 0.5 F_{TB} = \frac{F_d + F_g \sin(\theta) + 0.3 F_g \cos(\theta) + ma}{4}$$

Now, finally, the required output torque and mechanical power, for each motor, can be found by equations (2) and (3), respectively.

$$\tau = \frac{1}{2} d * F_T$$

$$P_{mech} = \tau * \omega = F_T * v$$

Where ω is the angular velocity of the wheel in rad/sec, and v is the vehicle velocity along the slope. This gives us the required motor specifications shown in Table C.1, for vehicles with 11 inch wheels.

Table C.1.: Motor Specifications				
	Terrestrial Prototype		Lunar Vehicle	
θ	Single Vehicle (Typical)	Towing Dead Vehicle (Extreme)	Single Vehicle (Typical)	Towing Dead Vehicle (Extreme)
0°	$F_t = 14.7150 \text{ N}$ $\tau = 2.0557 \text{ Nm}$, 291.1097 oz-in $P_{mech} = 7.3575 \text{ W}$	$F_t = 29.4300 \text{ N}$ $\tau = 4.114 \text{ Nm}$, 582.2 oz-in $P_{mech} = 14.7150 \text{ W}$	$F_t = 1.8281 \text{ N}$ $\tau = 0.2554 \text{ Nm}$, 36.1662 oz-in $P_{mech} = 0.9141 \text{ W}$	$F_t = 4.2813 \text{ N}$ $\tau = 0.5981 \text{ Nm}$, 84.6968 oz-in $P_{mech} = 2.1406 \text{ W}$
5°	$F_t = 18.9340 \text{ N}$ $\tau = 2.6451 \text{ Nm}$, 374.5748 oz-in $P_{mech} = 9.4670 \text{ W}$	$F_t = 37.8680 \text{ N}$ $\tau = 5.2902 \text{ Nm}$, 749.1 oz-in $P_{mech} = 18.9340 \text{ W}$	$F_t = 2.3523 \text{ N}$ $\tau = 0.3286 \text{ Nm}$, 46.5355 oz-in $P_{mech} = 1.1761 \text{ W}$	$F_t = 5.3295 \text{ N}$ $\tau = 0.7445 \text{ Nm}$, 105.4355 oz-in $P_{mech} = 2.6648 \text{ W}$
10°	$F_t = 23.0089 \text{ N}$ $\tau = 3.2143 \text{ Nm}$, 455.1891 oz-in $P_{mech} = 11.5044 \text{ W}$	$F_t = 46.0178 \text{ N}$ $\tau = 6.4287 \text{ Nm}$, 910.4 oz-in $P_{mech} = 23.0089 \text{ W}$	$F_t = 2.8558 \text{ N}$ $\tau = 0.3993 \text{ Nm}$, 56.5506 oz-in $P_{mech} = 1.4293 \text{ W}$	$F_t = 6.3420 \text{ N}$ $\tau = 0.8860 \text{ Nm}$, 125.4658 oz-in $P_{mech} = 3.1710 \text{ W}$
15°	$F_t = 26.9087 \text{ N}$ $\tau = 3.7591 \text{ Nm}$, 532.3392 oz-in $P_{mech} = 13.4543 \text{ W}$	$F_t = 53.8173 \text{ N}$ $\tau = 7.5183 \text{ Nm}$, 1064.7 oz-in $P_{mech} = 28.1107 \text{ W}$	$F_t = 3.3430 \text{ N}$ $\tau = 0.4670 \text{ Nm}$, 66.1354 oz-in $P_{mech} = 1.6715 \text{ W}$	$F_t = 7.3110 \text{ N}$ $\tau = 1.0213 \text{ Nm}$, 144.6353 oz-in $P_{mech} = 3.6555 \text{ W}$

Appendix D: Linking Arm and Envelope Studies

For the design of the linking envelope's front plate, sheet metal was selected because its relatively lightweight and inexpensive. SolidWorks simulation (FEA) was used to select the thickness of the sheet metal, as shown in Figure D.1. For the simulation, a 240 N load was placed on the envelope, representing the full weight of a SHREW. This scenario was simulated for several thicknesses of Aluminum 5052, as well as ABS plastic sheeting. The max von Mises stress and resulting safety factors are shown in Table D.1. Based on these simulations, 0.08" aluminum sheet metal was selected.

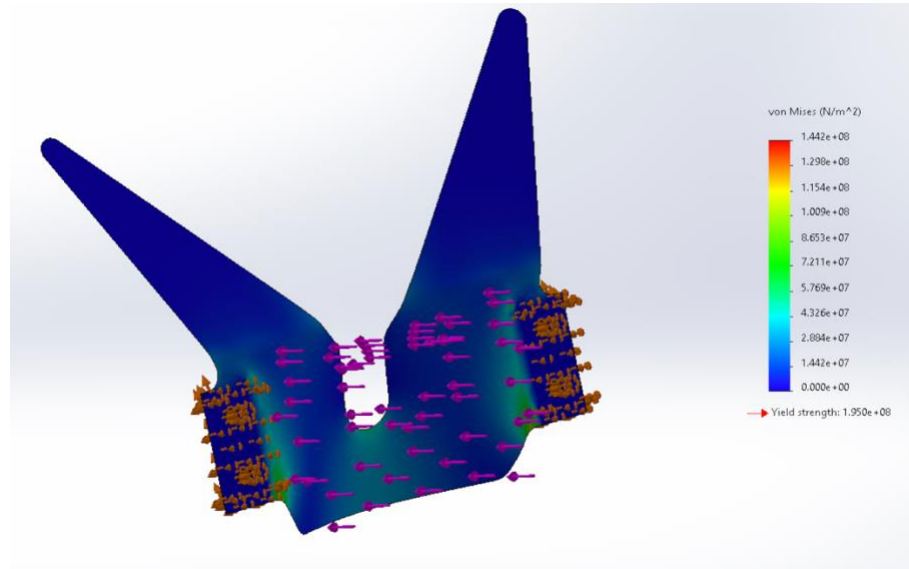
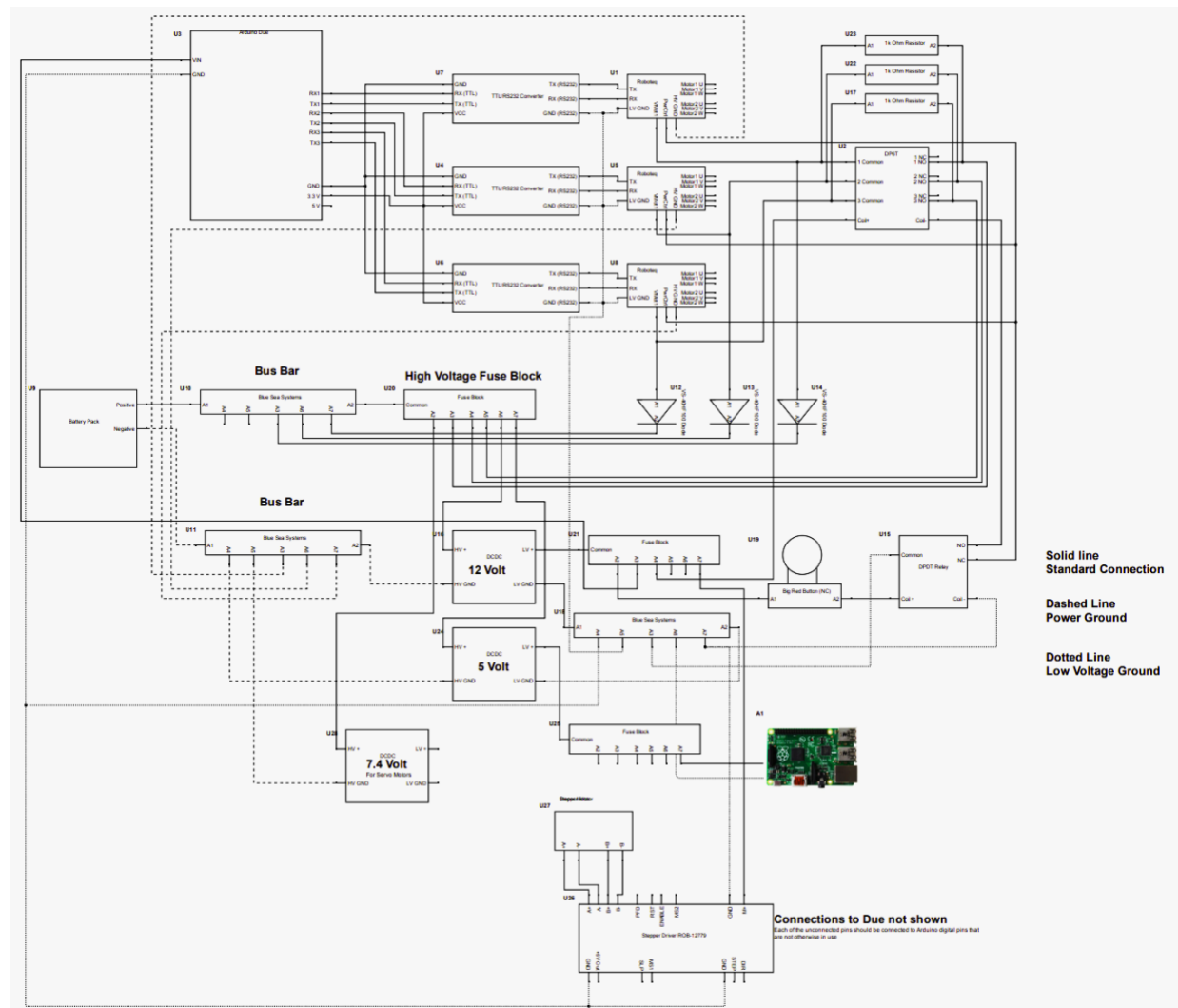
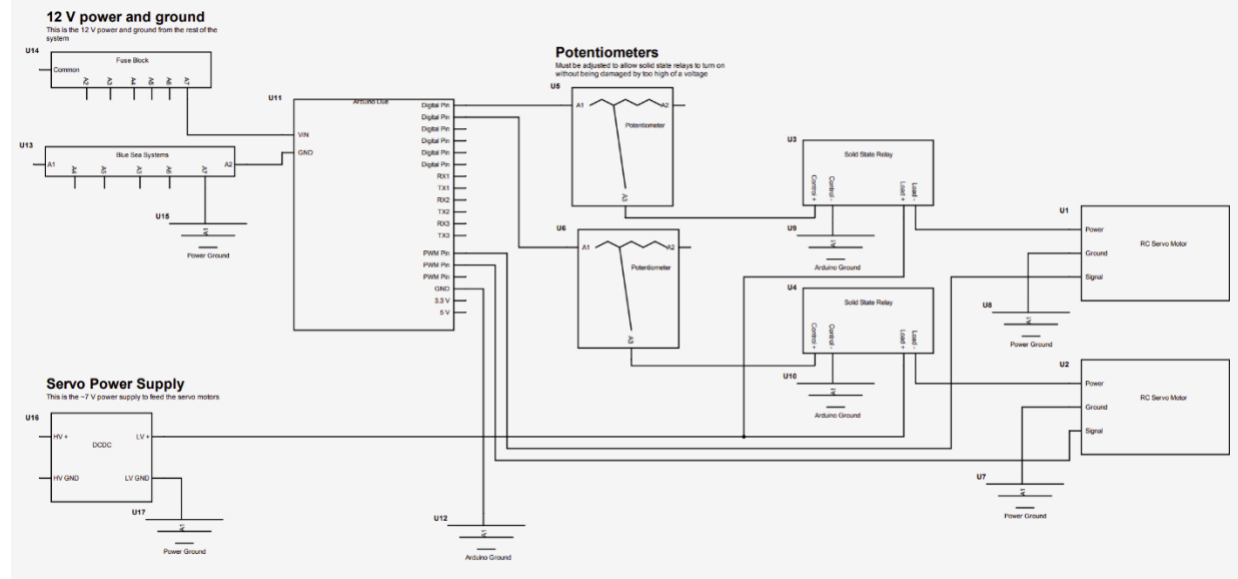
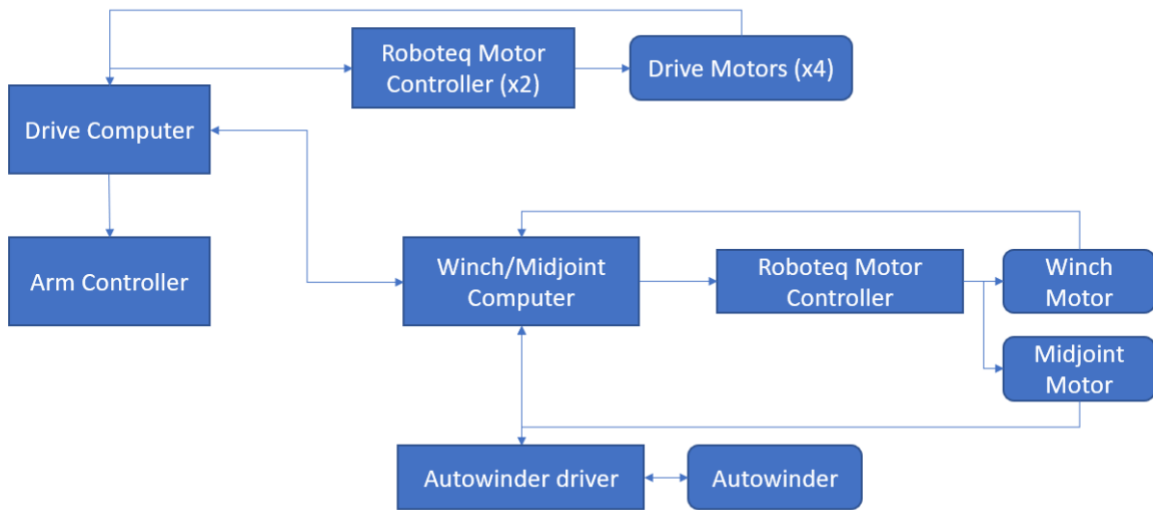


Figure D.1.: SolidWorks simulation for linking envelope

Table D.1. Simulation Results, Selected Design Highlighted in Yellow.				
Material	Thickness (in.)	Max Von-Mises Stress (MPa)	Yield Strength Safety Factor	Mass (g)
Aluminum 5052	0.08	53.6	3.6007	198
Aluminum 5052	0.063	85.8	2.2494	158
Aluminum 5052	0.05	134.8	1.4318	124
ABS Plastic	0.125	22.3	0.9596	109
ABS Plastic	0.1875	10	2.1400	165
ABS Plastic	0.25	6	3.5667	219

Appendix E: Electrical Diagram





Appendix F: Thermal Calculations

To simulate the thermal stress on the WEB we used a numerical methods simulation to calculate the transfer of heat within the system every 10 seconds. We assumed that: the total surface area of the outer box would be 0.3m^2 to completely encapsulate the inner box which has a surface area of 0.2m^2 ; the inner and outer boxes are cubes; the inner and outer boxes, the electronics, and the wax are lumped systems with uniform temperatures due to the length of the time step; the inner box is made entirely of titanium which has a lower heat capacity than Teklam; the electrical components inside the WEB were made of silicon; during the lunar day sunlight is incident on half of the WEB; blackbody radiation from the moon would only be incident on $5/6$ of the surface area of the outer box; the solar irradiance during the lunar day would be $1361\text{ (W/m}^2\text{)}$ which is the average solar irradiance at one astronomical unit from the sun; during the lunar day the surface temperature of the moon is 400K which is the maximum recorded temperature on the moon; during the lunar night and in the PSR the surface temperature of the moon is 41K which is consistent with temperatures recorded in PSRs; the internal electrical components dissipate 8W of power as heat; the aerogel has a thermal conductivity of 0.004 (W/mK) ; the aerogel layers are 8cm thick; and the paraffin wax heat exchanger, inner box, and the electronics are thermally coupled. From these assumptions the simulation was able to predict the thermal behavior of the WEB.

At each time step the model calculates the change in temperature for the outer and inner boxes of the web using a Euler forward algorithm. The model first determines if it is currently day or night based on the current time step. If the model determines that it is currently the lunar day, it calculates the change in temperature accounting for the solar irradiance and the daytime lunar surface temperature. If the model determines that it is the lunar night or that the rover is in the PSR, then it will calculate the change temperature accounting for no solar irradiance and the nighttime lunar surface temperature. The primary drivers in the change in temperature for the outer box are the heat flux from: solar irradiance, radiation emitted by the surface of the moon, radiation emitted from the inner box, conduction through the aerogel to the frame of the rover, and radiation from the outer box itself. To calculate the change in temperature for the inner box, the model considers the heat flux from: the heat produced by the electronics, the radiation emitted from the outer box directed towards the inner box, conduction between the outer box and the inner box through the aerogel, and radiation away from the inner box.

With no atmosphere on the moon the only methods of heat transfer that we need to consider are radiation and conduction. With the use of highly insulative materials such as Aerogel, the effects of conduction can be extremely diminished. All components in the WEB will emit blackbody radiation of a given intensity which can be changed by the careful selection of materials and coatings with specific absorptance and emittance characteristics. In order to calculate the radiation emitted by each element we used the Stephan-Boltzmann Law

$$P = \epsilon A k_b T^4$$

where P is emitted power, A is the surface area, ϵ is the emissivity of the material, k_b is the Stephan-Boltzmann constant, and T is the absolute temperature of the emitting body. The radiative power absorbed by each body is calculated by

$$P_A = P_I \alpha$$

where P_A is the thermal power absorbed by the material, P_I is the thermal radiation power incident on the material, and α is the absorptance of the material. To calculate the conduction through the aerogel we treated the aerogel as a lumped thermal resistor. The heat transfer between the two boxes and the outer box and the frame is defined by

$$Q = (T_1 - T_2) k_c \frac{A}{L}$$

where Q is heat flow, T_1 and T_2 are the temperatures of the two bodies; and k_c is the thermal conductivity, A and L are the area and thickness of the thermal resistor.

Once the heat flux of the system was calculated, the change in temperature of each component is determined by accounting for the specific heat of the different materials and the time step. We keep track of the current state (solid, liquid, or phase change) of the paraffin wax and used the appropriate specific heat value to determine its change in temperature. When the wax reaches its melting point, we then keep track of how much energy is needed to completely melt or freeze the wax before adjusting its temperature and the temperature of the components it was coupled with.

Using this model, we were able to simulate the potential thermal stress on the system over a mission of any specified length. The material thermal characteristics of the WEB are detailed below.

Material	Specific heat capacity (J/kg•K)	Heat of fusion (J/kg)	Mass (kg)	Absorptance	Emittance	Thermal conductivity (W/m•K)
Aluminum Foil	921.1	N/A	0.025	N/A	N/A	N/A
Titanium Coating	520	N/A	0.25	0.52	0.12	N/A
Paraffin Wax	Solid: 2900 Liquid: 2130	230000	1.0	N/A	N/A	N/A
Silicon	710	N/A	2.0	N/A	N/A	N/A
Aerogel	N/A	N/A	0.027	N/A	N/A	0.004
Barium Sulfate with Polyvinyl Alcohol Coating	N/A	N/A	N/A	0.06	0.88	N/A
AgBeCu with Parylene C Overcoating	N/A	N/A	N/A	0.22	0.34	N/A
Lunar Surface	N/A	N/A	N/A	N/A	0.9	N/A

Appendix G: Teklam Beam Calculations

A primary design constrain of our proposed solution is a payload mass of 15 kg., as Commercial Lunar Payload Services and their landers currently in development have limited mass capacity. The estimated cost of transport to the lunar surface is \$1 million per kilogram. Naturally, it is of high priority for our team to reduce weight. Simultaneously, our set of rovers must stay sufficiently large to maintain traction. For this reason, we must consider novel, lightweight materials to provide the structural elements of the vehicle.

Currently, the shape of our vehicle chassis is arbitrary. That said, we have a basic understanding of the load types our vehicles will likely experience. Likewise, the robots previously produced in our lab all contain a similar feature in their chassis, despite only one being made from Teklam. At the head and tail of each vehicle is a beam-like section which contains the motors, gearheads, and bearings for each pair of wheels (the second vehicle, Yeti, is further subdivided into a separate beam-like section for each drivetrain individually). For these reasons, and for those described above, I will study box-section sandwich beams, sized to contain our motors and gearheads. The exact shape of our frame will certainly change many times in the coming months. So, studying a simplified shape, with a general morphology known to be effective, will be incredibly meaningful as an informative tool for our group, as we move further into prototyping. The design of our vehicle frame must be capable of withstanding high compressive loading through the span of the frame, while remaining sufficiently light. Due to the many undetermined factors to which our design is reliant on (CLPS lander specifics, frame morphology, supported testing equipment), our analysis on materials must be general enough to provide meaningful information regardless of specifics. Flexural testing of box-section sandwich beams can provide us with informative metrics on this front, in the form of flexural rigidity and elastic moduli.

Background

In the past, Dr. Ray's lab employed a sandwich core material commercially known as Teklam, among other names, in the construction of a lightweight box-frame for their first Artic rover, Cool Robot. This is shown in Figure 1. The material was also used to construct outriggered mounting points for a solar panel lid.

In general, a sandwich panel is any structure made of a low-density interior mechanically bonded to thin face sheets on either side. The use of such panels is widespread and popular due to their material properties, particularly in aircraft where weight savings are critical, as was the case with Cool Robot. The average reader has most likely experienced this material in the overhead storage containers on commercial airlines. The specific panel type selected for Cool Robot was chosen for its high structural rigidity, low weight, relatively low cost compared to other panel types and insulating properties. The material features a lightweight honeycomb Nomex core, laminated between two thin fiberglass sheets, as shown in the close-up of Figure 2a. Alternatives exist in which the face laminates are replaced by carbon fiber or aluminum. Presently, our lab has access to standard ¼" Teklam, which will serve as the primary material of consideration in later sections. Material properties are included in "Teklam P/N NE2G102250 Product Data Sheet." in the References section and as Appendix 2. All things considered, the engineering evaluations our lab has previously completed on this material are limited. In 2004, Alexander Price discussed the material in the

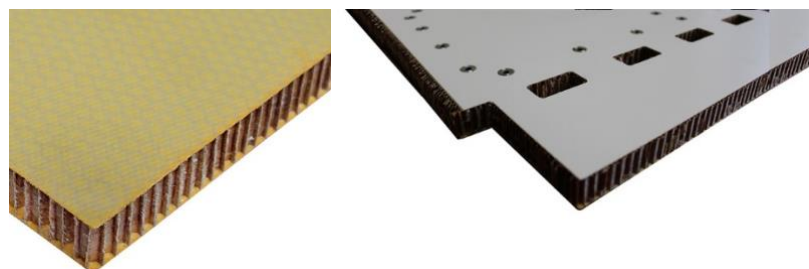


Figure 2: a.) Standard ¼" Teklam, #NE2G1-02-250 {N502E} b.) An example of Rockwell Collins' aeroADD™ value added operations, which includes fixture inserts and embedded detail ("aeroADD™").

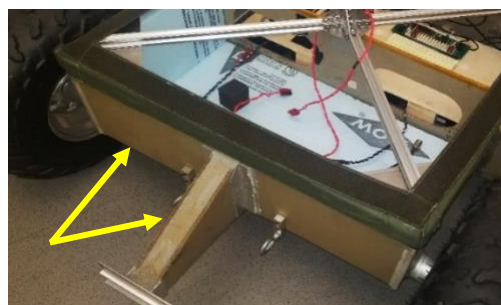


Figure 1: Arrows indicate sandwich panels which form the box-frame and outriggers on Cool Robot.

construction of Cool Robot as part of his undergraduate honors thesis. He simply noted, however, that the material is likely strong enough and light enough for their applications, without performing any substantial evaluations. This resulted in a frame which was initially poorly-suited to resist the loads experienced in the Antarctic and Artic, and, as a result, aluminum cross bars had to be added to the main diagonals of the robot in order to support the box (Price 57).

Similarly, ispace, a lunar exploration company, used sandwich panels in their construction of a 3.8 kg. lunar vehicle named Sorato, which was later selected for the prestigious Google Lunar XPRIZE competition. In particular, they used a panel with a 3.5mm Nomex honeycomb core, reinforced on the faces with a carbon fiber polymer (Walker). Finally, several other concepts developed under the same Lunar XPRIZE competition used honeycomb panels. This makes honeycomb sandwich panels an obvious candidate for use in the construction of our vehicle chassis. Additionally, carbon fiber is a candidate of consideration, and as we engineer Earth analogues of our BIG Idea vehicle, aluminum becomes a candidate of consideration, as well, due to scaling with gravity.

Load testing of these sheets is not uncommon. For example, R.Roy et. al. used an Instron 5582 model load press to test the tear-out strength of value added, through-the-thickness bolt inserts [6]. These tests were done to ASTM standard C297. All tests I perform will likely be done to the same ASTM standards. For CFRP Nomex sheets. They found that for a 3-Ply specimen that there are distinctive transition zones that occur as the pull-out load increases. This is a result of the Nomex core buckling. Up to displacements of 3.5mm, the samples were stable, taking on a load of ~3.4kN. That said, they identify a first-failure zone as the location for which pull-out testing results in a 2% deviation from the initial loading regression and when permanent damage states to occur. This was at 893N for the 3-Ply sheet (Roy et. al). That said, these tests were performed on CFRP Nomex sheets and our lab has access to Fiberglass Nomex sheets. Other words relevant specifically to sheet properties are found in (Giglio, M., et al) and (Qiao, P, et al). Specifically, Pizhong Qiao and others describe in great detail the dynamical equations governing sheets, in terms of layer density and internal stresses. I hope to use these governing equations to develop beam structures suited to resist the loads we expect to experience. From what I am uncovered load testing of honeycomb sheets is frequent. That in mind, I have found no works to date analyzing how these composite structures behave as part of larger more complex structures like enclosed beams.

Loading

Oddly enough, analysis of our vehicle must begin from the ground up, because it is from the below the vehicle where most loads will originate. Ph.D. candidates Joshua Elliot and Austin Lines, of Dr. Ray's laboratory, previously developed a vehicle, known as Frosty Boy, for the research and recovery in Arctic Regions. It is by far the most stable platform in terms of reducing instances of immobilization. On a flat surface on Earth, it exerts a ground pressure of roughly 0.35 PSI, at roughly 100kg. This means each wheel distributes its load over ~155 in². It seems fitting to scale this to our 15 kg. vehicle. seeking to maintain the same ground pressure in the lunar environment. From this, we can then evaluate this scenario by considering what load will be exerted on the vehicle from the environment. This informs material selection. Likewise, although our vehicle will likely never be shipped to the Moon itself, we must consider the added, virtual gravity such a vehicle will experience on deployment to the lunar surface. This is largely consequential to the design and descent rate of the landers being developed under NASA's Commercial Lunar Payload Services (CLPS). That said, specifics on the morphology of the interior space where the robot will reside, in addition to the maximum thrust upon landing, are presently unknown, as the landers are still in the development phase. Finally, because our concept involves small rovers capable of pulling small loads, the frame of our vehicle must be capable of withstanding tensile stress due to drawbar pull through the frame.

I anticipate that of the three loading types our vehicle will experience, force due to gravity, force due to drawbar pull, and force due to trust on descent, the lattermost load will be the most substantial. This is because the body-forces associated with a 15kg mass on the Moon will be next to negligible in terms of the impact on the material we select. Likewise, because the size of our rover will be particularly small, the expected drawbar pull for which we can produce stable tractive forces is also limited. As such, we desire an informative metric of flexural strength of candidate materials, to gain an understanding of the loads each material can withstand. Then, as information of the CLPS landers is revealed in the coming months, we may select a frame material which meets the needed strength. The remainder of this report assumes that loading is almost entirely compressive, applied vertically through the span of our frame.

Preliminary Analysis

I began my initial "by hand" analysis of enclosed Teklam beams by asking what shape will be the lightest. Assuming arbitrary but equivalent beam lengths, max bending moments, max bending stresses, and material properties, I looked at three candidate cross-sectional types, triangular square, and trapezoidal. In this evaluation, ultimately what we are considering is that all three types will share section moduli, $S = \frac{M}{\sigma}$. Figure 3 shows the shapes

I started from; the full evaluation is attached as Appendix 3. While it may have been easier for me to assume that there is no overlap within the cross-section, this would be highly unrealistic because of the added strength due to additional epoxy and one wall which is doubly thick.

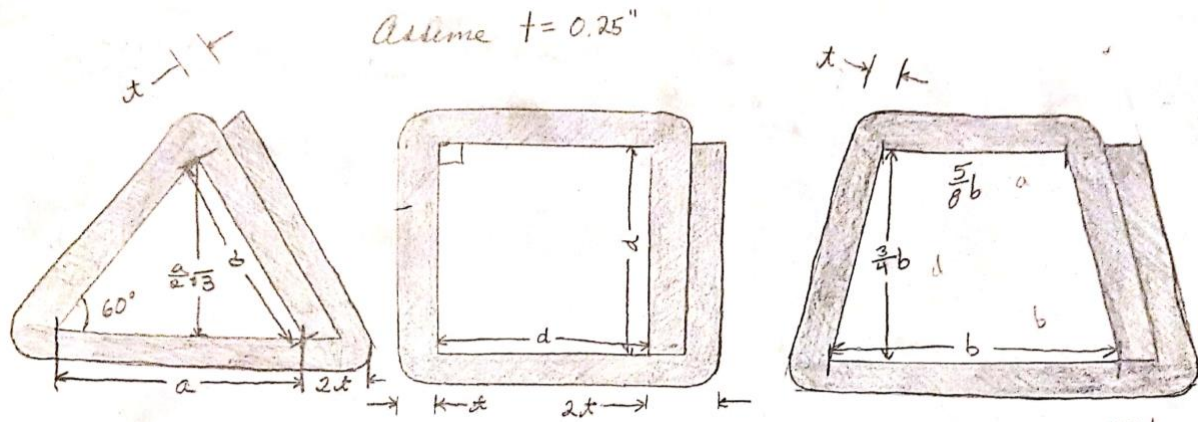


Figure 3: Candidate Cross Sections for weight evaluation by section modulus.

We write the section modulus in terms of the undetermined inner dimensions a , d and b , respectively and assume a wall thickness of $0.25''$. Then, having written expressions for the section modulus of each beam, we use this to solve for the inner dimension, followed by using this to calculate the cross-sectional area which the beam occupies, excluding the interior, as it does not constitute any weight. I should note that at this point, one will realize there is no analytical solution for the inner dimension of the trapezoid. As such, I did not continue considering the trapezoid from here, on, largely because we are unlikely to use such a shape to begin with.

Now, we have expressions for area in terms of the section modulus, and, as such, we plot the section area as a function of varying section moduli. This shows then that, assuming the triangular beam and the square beam are of proper size to share max bending moments, max shear stress, poisson ratios, and lengths, the triangular beam will, in fact, be lighter. The cross-sectional area vs. section modulus plot is shown in Figure 4. While this may seem counterintuitive, it is likely a consequence of the impact of the overlapping wall.

Now, knowing what we presently know about the construction of enclosed sandwich beams, we found that bending sheets beyond ~ 110 degrees will result in facturing of the exterior facing. From this, we now know the creation of a triangular beam from Teklam, will not end well (trust me, I've tried.). While this is unfortunate, it is also not the end of the world, because if we were to construct sections large enough to contain a part of a certain size (say a motor; this is ultimately what I chose to do) the triangular beam will still be heavier. It is only in the case where the beam is not sized to contain a certain piece, and all else is equal, that the triangular beam is lighter.

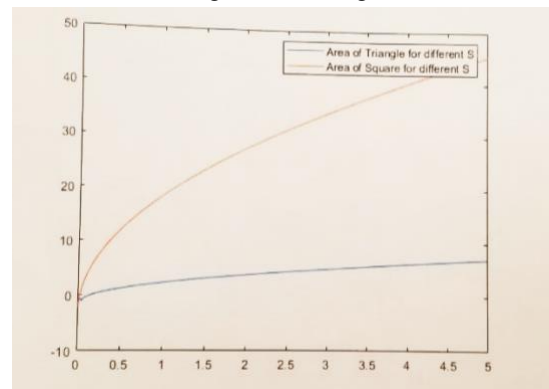


Figure 4: Plot demonstrating the lower mass of a triangularly enclosed beam.

Construction of Box-section Sandwich Beams

Collins Aerospace offers value added operations to manufacture more complex structures from flat sheets (“aeroADD™”). By using CNC machines, ovens and custom tooling they are capable of inserting fixture components, sealing edges, embedding fine detail into the panel, and finally folding the panel into three dimensional structures (Figure 2b provides an example of available operations). That said, it is often impractical to prescribe such services in scenarios where the component being manufactured is not a final version, few parts are needed, or the costs outweigh the benefits. This is the present case for our group, as we are only looking at enclosed beam-structures as an informative tool for further development of the chassis, not looking at the chassis itself.

In the coming months, should we select Teklam as a material more suited than alternatives for our application, it may be appropriate to contact Rockwell Collins to get a sense of the cost to manufacture several half chassis/frame components. As outlined on their website, these custom shapes may be designed to meet the FAA’s flammability requirements, which could potentially be extended to meet the thermal requirements of the Lunar South Pole (likely

with some provided insight from our team on potential mating resins or alternatives to standard Nomex). Similarly, customers can provide Collins with custom tooling to generate the form they desire in a more experienced, professional setting.

For our present purposes, this is far beyond our means, needs, and desires. As an alternative, I was able to construct a test section of an enclosed square beam with a one side overlap. The remainder of this section describes the simple method for constructing three dimensional forms from flat sheets, with this shape as the example.

1. First, begin by determining the shape and size of the structure. In our case, we desire a cross-section of an enclosed beam sufficiently large to contain the mounting block of our motor (this is where the motor is widest). Such a cross-section is shown in Figure 5
2. Transform the three-dimensional structure into a plan for a flat sheet. When making this transformation in your design, corners will be constructed from removing a thin strip of the facing material, on the side you are bending toward. Removing a thin strip and bending away from the same face will result in the facing cracking. The width of this thin strip is proportional to the thickness of the sandwich and the desired angle by arch length formula. For example, for a $\frac{1}{4}$ " sheet bent at 90° should require a strip ~ 0.39 " wide. In practice $\sim 5/16$ " was sufficient. Making the strip slightly smaller reduced the gap once folded. It's recommended that you begin with a small test piece to the calculated width and adjust from there. On a similar note, we experienced that bending any further than $\sim 110^\circ$ began to compromise the fiber glass facing.
3. Transfer your plan to the sheet and remove strips where desired. For the construction of our test beam, I used both a rotary tool and a box cutter paired with a metal straight edge to remove the facing material. Of these, the box cutter was more effective. If your desired shape is complicated, a CNC mill is recommended. The depth of material removed should increase as the length of the fold increases. This is because the resistance due to bending is greater for a longer folded edge. For edges less than 1 foot long, we found that removing just the facings was effective. For sections longer than this, I cut a shallow V into the Nomex interior to make folding easier, as shown in Figure 6

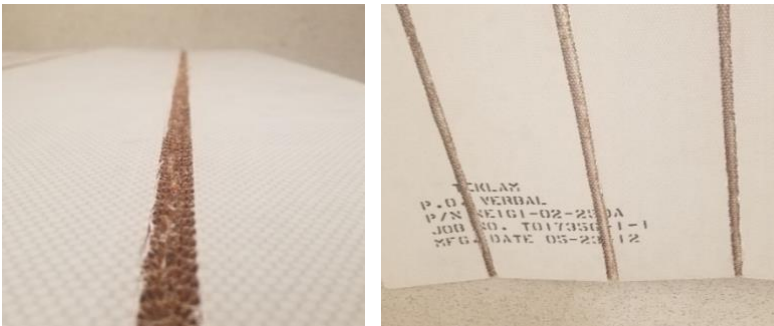


Figure 6: V-cuts removed to establish joint locations.

knife. This step is incredibly important if the internal dimensions of your structure are of significance, as otherwise the excess epoxy will spill out of joints and harden, changing the internal dimensions.

6. Fold your structure into its final shape and clamp into place. This step will likely require a form, jig, or similar piece to ensure your part sets in the appropriate shape. We used several thin wooden blocks on the inside of the layup to keep the inside square and to ensure that the beam did not splay at the seam. These blocks were later easily removed with a mallet and a lengthy drill bit. Keep in mind that if you wish to use the same form multiple times, it is in your best interest to allow the epoxy to slightly set and then remove it. Any sooner and your final layup will contain gaps where there should be none. Any later and your form may need to be destroyed in order to be removed. In the clamping of your section, the more distributed the clamping force, the better the final layup. It was effective for our team to clamp the section shut with a plethora of zip-ties, as shown in Figure 7.

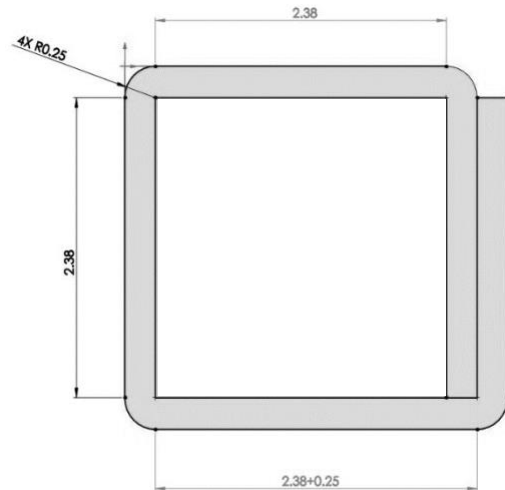


Figure 5: Desired cross-section of enclosed square honeycomb beam.

4. Test folding into the desired shape. Adjust as needed.

5. Apply a 2-part adhesive to the exposed Nomex core, filling the honeycomb as much as possible. For our beam section, we used Metalset A4 Aluminum Epoxy Resin Cement. It was also used between the faces of our overlapping wall to seal the section shut. We filled all exposed strips, folded once, then unfolded to scrape away excess with a putty

7. Finish by removing any excess epoxy and ensuring your part is square where desired.

It is also worth noting that because this material is orthotropic, our beam is constructed with its length being perpendicular to the length of the full sheet. In other words, the interior honeycomb is oriented such that the Nomex ribbons forming the honeycomb run along the length of the beam. This is considered the ‘L’ dimension in the field of sandwich beam testing. The perpendicular direction is considered the ‘W’ direction.

Testing Format Standard

Our testing method follows a modified sandwich beam procedure to determine the ‘core’ shear properties by beam flexure. We use standard C393/C393M of the American Society for Testing and Material (ASTM) (“Standard Test Method for Core Shear Properties of Sandwich Constructions by Beam Flexure.”), which we modify to the properties of our beam. Standard D7250/D7250M is then used to determine the flexural and shear stiffness (“Standard Practice for Determining Sandwich Beam Flexural and Shear Stiffness.”).

C393 is a standard test method to determine core shear properties of sandwich constructions subjected to flexure “in such a manner that the applied moments produce curvature of the sandwich facing planes.” Typically, this standard is only used on flat constructions. For our purposes, this test method is modified such that the upper and lower walls of the enclosed beam, touching the loading points and support points, respectively, are treated as the ‘facings’ of our beam. Similarly, we treat the remaining walls and the hollow interior as the ‘core’. Make no mistake, there are likely better alternatives to characterizing the flexural properties of similarly constructed beams, however this seems like a suitable assumption to make, especially because, in the practice of this standard, the properties of the facings and the core are not entirely independent of each other, and, for this reason, the core shear properties are more representative of the member as a whole.

Apparatus & Configuration

We load our beam using a benchtop Instron 4469 loading frame with a 50kN load cell. Force was applied vertically through the loading bars with the support bars beneath it fixed. This is used to collect force versus deflection measurements, collected in SI units. Small buffer blocks were placed over the support and loading rollers to limit the impact of flatwise compression, which crushes the interior Nomex prior to reaching the yielding strength. This is in line with subsections 7.2.3 and 7.2.4 outlining the apparatus specifications of C393. While the rollers are of sufficiently large radius (>3mm), the method allows for roller widths of up to one inch and for pressure pads.

We tested under 3 the loading conditions: 3-point bending, 4-point quarter length bending, and 4-point third length bending shown in Figure 8, from the ASTM test method.

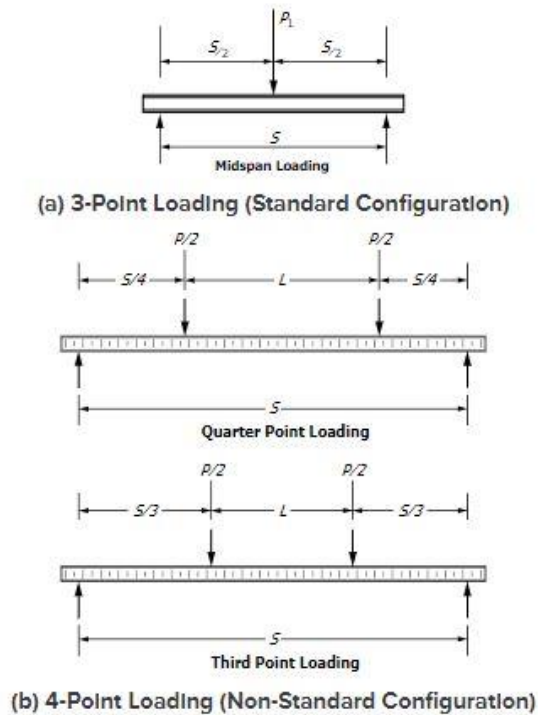


Figure 8: Loading Configurations Considered for Flexural Beam Test (“Standard Test Method...”).



Figure 7: Distributed clamping of enclosed beam section.

The support span length must satisfy:

$$S \leq \frac{2k\sigma}{F_s} + L$$

where S is the width of the supports, L is the loading span length, F_s is the estimated core shear strength, σ is the expected facing ultimate strength, k is the facing strength

factor (recommended $k=0.75$), and t is the facing thickness. We assume $k=0.75$, $\sigma=690$ MPa (the ultimate strength of fiberglass), and $t=0.25$ inches. Likewise, because our beam is particularly thick in comparison to the thicknesses assumed in C393, we set the span of our supports as large as possible. For our jig, $S_{max} \approx 15$ inches. Now, because the expected core shear strength is unknown, we select L so that the right-hand side of $F_s \leq \frac{2k\sigma t}{S-L}$ is much larger than the viable shear strength. Increasing L simply places us further from the threshold of the expected ultimate strength. For 4-point, quarter length loading S was set to 7.5 inches. For 4-point third length loading, our desired $S=5$ inches for $L=15$ inches, however the loading bars available to me at the Thayer School of Engineering could not be configured into a five-inch span. This in mind, our third length configuration was set to $S=4$ inches and $L=12$ inches. We can see, now, that even in limiting case of 4-point, third length bending, the right-hand side is equal to ~ 16.171 MPa, which is well beyond anything expected. Real-world images of each loading condition are presented in Figure 9.



Figure 9: a.) 3-point setup b.) 4-point, quarter length c.) 4-point, third length.

Sampling & Conditioning

Our previously constructed beam was cut into three, 16 inch sections. C393 dictates that at least five specimens are tested per test condition to achieve results of statistical significance. Because the layup process previously described is rather lengthy, this was beyond our means. That said, the standard allows results to be gained through fewer specimens in a designed experiment, which is what we are presently doing. Consequently, however, we chose to test each sample under each loading condition over three runs, for a total of nine data sets for each member and on each condition, 27 runs in total. This is still within line of ASTM practices, so long as each test is not done to the member's yield and the facing are not significantly compromised with in tests. This will provide us with robust data on the linear-elastic region of each member's bending. The final run on each member was done to the ultimate strength, one for each loading condition. A summary of the testing conditions is provided in Table 1, with each condition being performed in the order it is listed.

Table 1: Sampling of Each Member			
Member 1	Member 2	Member 3	Condition #
3-point, 3 runs	4-point, quarter; 3 runs	4-point, third; 3-runs	Test Condition 1
4-point, quarter; 3 runs	4-point, third; 3 runs	3-point, 3 runs	Test Condition 2
4-point, third; 2 runs	3-point; 2 runs	4-point, quarter; 2 runs	Test Condition 3
4-point, third; 1 run to failure	3-point; 1 run to failure	4-point, quarter, 1 run to failure	Test to Failure

Tests were performed at a rate of ~ 5 mm deflection per minute, resulting in a speed in compliance with 11.4 of C393.

Real World Data

Force (in kN) vs. deflection (in mm) plots are shown below for all non-failing runs in Figure 10. Note – during these runs, the perceived drop in load near the tail end is a result of collecting data after the run has stopped, not as a consequence of a detected failure. The change in the slope of the linear elastic region in run 3 of the 4-point, third length test, on beam 2 (the middle, bottom figure) is a result of the facing slightly cracking directly beneath the load points, not failure due to bending. Figure 11 presents the final three runs, all to failure.

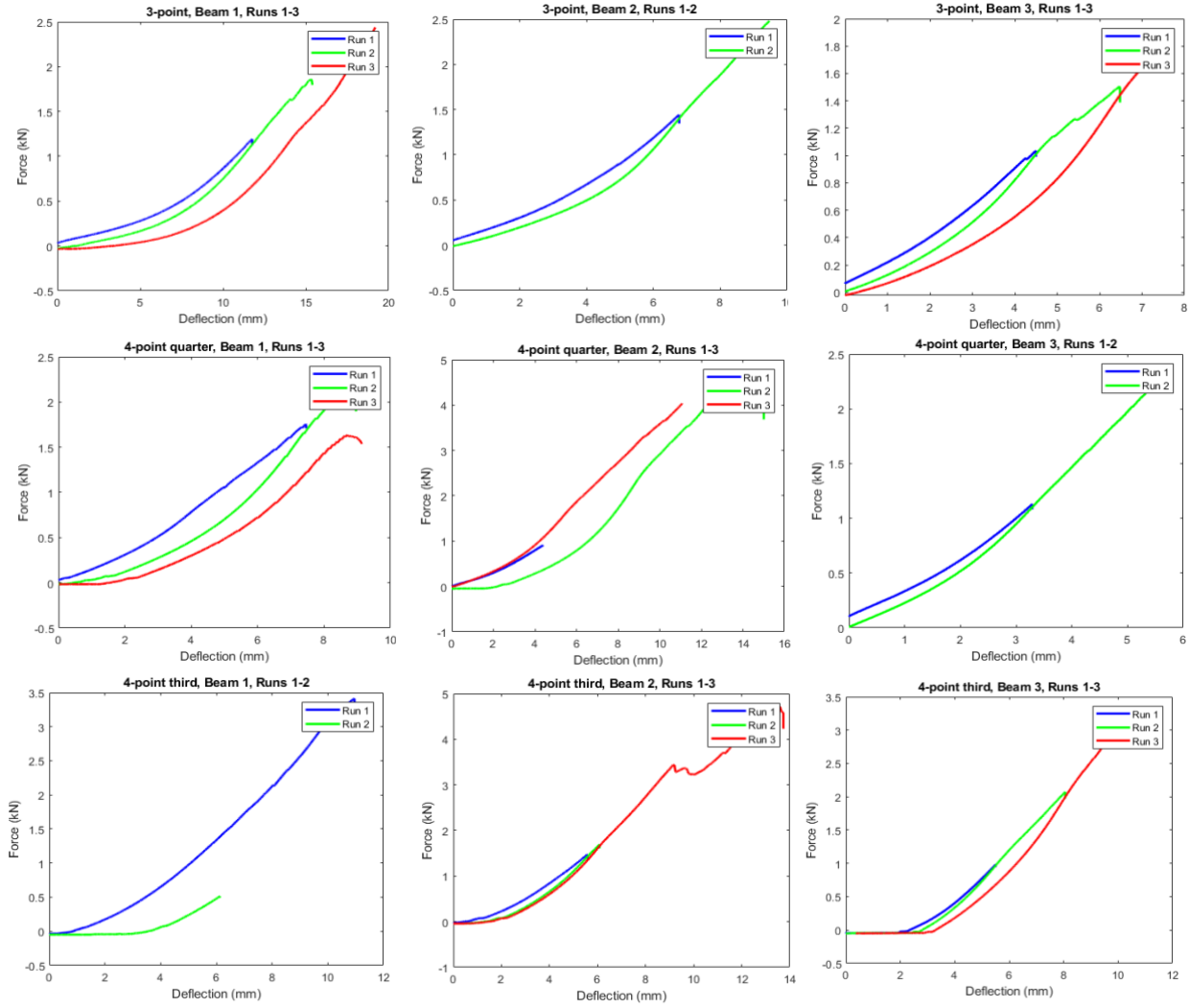


Figure 10: Force vs. Deflection Curves for the 24 non-failure runs.

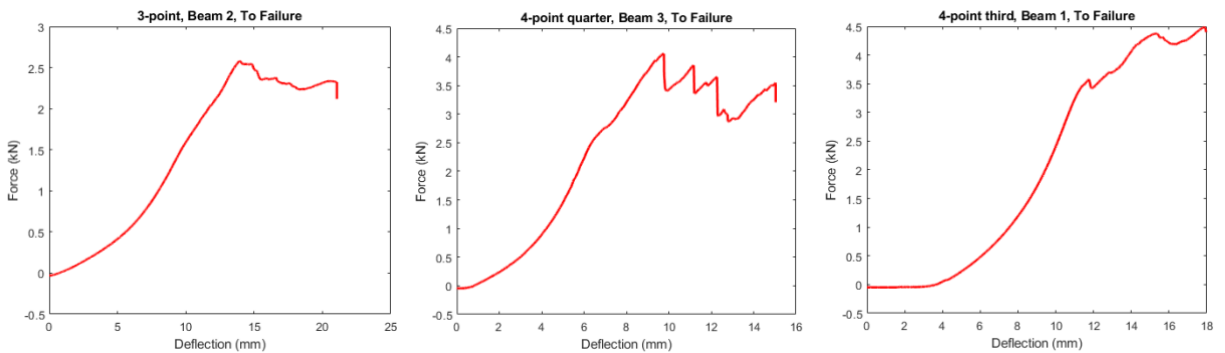


Figure 11: Force vs. Deflection to failure of each member, 1 under each loading condition.

Results and Evaluation

From each run above, we began by isolating the linear elastic region such that we could extract the bending rigidity and the elastic modulus. Transition points were identified by a 10% deviation from the slope of this region. Reported in Table 2 is the average bending rigidity (with the deviation from linearity within the region) and elastic modulus from each run.

Table 2		
3-point Runs	Bending Rigidity (N/m)	Elastic Modulus (MPa/m)
Beam 1, Run 1	3.3*10 ³ , R ² =0.9927	.5696
Beam 1, Run 2	3.5*10 ³ , R ² =0.9913	.6041
Beam 1, Run 3	4.2*10 ³ , R ² =0.9934	.7249
Beam 2, Run 1	5.1*10 ³ , R ² =0.9985	.8802
Beam 2, Run 2	6.7*10 ³ , R ² =0.9996	1.1564
Beam 2, Run 3	4.3*10 ³ , R ² =0.9982	.7422
Beam 3, Run 1	3.6*10 ³ , R ² =0.9885	.6214
Beam 3, Run 2	4.2*10 ³ , R ² =0.9823	.7249
Beam 3, Run 3	6.4*10 ³ , R ² =0.995	1.1047
Average	4.589*10 ³	.7940
4-point Quarter Runs		
Beam 1, Run 1	4.2*10 ³ , R ² =0.9922	.7246
Beam 1, Run 2	6.7*10 ³ , R ² =0.9959	1.1558
Beam 1, Run 3	5.2*10 ³ , R ² =0.9878	.8971
Beam 2, Run 1	4.3*10 ³ , R ² =0.9979	.7418
Beam 2, Run 2	7.1*10 ³ , R ² =0.9926	1.2249
Beam 2, Run 3	8.2*10 ³ , R ² =0.9957	1.4147
Beam 3, Run 1	4.9*10 ³ , R ² =0.9873	.8436
Beam 3, Run 2	8.4*10 ³ , R ² =0.9995	1.4492
Beam 3, Run 3	9.2*10 ³ , R ² =0.996	1.5872
Average	6.467*10 ³	1.1157
4-point Third Runs		
Beam 1, Run 1	6.4*10 ³ , R ² =0.9933	1.1041
Beam 1, Run 2	3.4*10 ³ , R ² =0.9891	.5866
Beam 1, Run 3	10.2*10 ³ , R ² =0.9905	1.7597
Beam 2, Run 1	5.6*10 ³ , R ² =0.9924	.9661
Beam 2, Run 2	7.2*10 ³ , R ² =0.9895	1.2421
Beam 2, Run 3	9.3*10 ³ , R ² =0.9984	1.6045
Beam 3, Run 1	5.6*10 ³ , R ² =0.9927	.9661
Beam 3, Run 2	5.1*10 ³ , R ² =0.9997	.8802
Beam 3, Run 3	5.3*10 ³ , R ² =0.9982	1.0388
Average	6.455*10 ³	1.1137

3-point Stress calculations

For the 3-point mid span loading, we found the max core shear stress from:

$$\sigma_{max} = \frac{F_{max}}{(d + c)b}$$

where σ_{max} is the core shear stress, F_{max} is the maximum force prior to failure, d is the overall thickness, c is the core thickness, and b is the width of the member. Similarly, the core yielding stress is found from replacing the included force with the yielding force and the stress on the facings is found by

$$\sigma_{facing} = \frac{S \cdot F_{max}}{2t(d+c)b}$$

The yielding force and maximum force are found from the third run on Beam 2 as $F_{yielding} = 1.627\text{kN}$ and $F_{max} = 2.579\text{kN}$, respectively. This gives us a max core shear stress of $\sigma_{max} = 9.582\text{ MPa}$, the core yield stress of

$\sigma_{yield} = 6.0517$ MPa and a facing stress of $\sigma_{facing} = 287.78$ MPa. It is worth noting that the facing stress is simply a reference value at the maximum applied force and does not represent the facing ultimate strength, as described in C393.

4-point quarter span stress calculations

The max core shear stress and the core yielding stress for 4-point, quarter span bending use the same equations as in the 3-point case. From the third run on Beam 3, we found yielding occurred at a force of $F_{yielding} = 2.737$ kN and the max force prior to failure was $F_{max} = 4.058$ kN. This results in $\sigma_{yield} = 10.1804$ MPa and $\sigma_{max} = 15.0939$ MPa. The facing bending stress is now found from the same equation as in the 3-point loading case, with the coefficient changing from $\frac{1}{2}$ to $\frac{1}{4}$. This gives $\sigma_{facing} = 226.4086$ MPa.

4-point third span stress calculations

Finally, we find the same values as in the other cases, but the $F_{yielding} = 3.576$ kN and $F_{max} = 4.486$ kN coming from run 3 on Beam 1. Likewise, the coefficient in the facing stress equation becomes $\frac{1}{3}$. From this, $\sigma_{yield} = 10.1804$ MPa, $\sigma_{max} = 15.0939$ MP and $\sigma_{facing} = 226.4086$ MPa.

Discussion and Conclusions

In my opinion, future groups in our lab or others considering similar options should only move forward with rigorous work and development on honeycomb panels if they are already nearly convinced of a fit for their application. This is because in a university setting, value added operations will likely be done in-house to limit the cost of manufacturing. As a result, one will be tasked with a time intensive layup, as described herein. Keep in mind the shape we constructed is relatively simple. More complex structures require more complex forms and more elaborate clamping, and thus more time. While the method itself is very easy to understand, I personally believe, having done it myself, that such a layup is more time than it is worth, unless the mass savings are of highest priority and alternative materials seem ill-suited for the application.

Likewise, we found that in the loading of these constructed beams that certain, undesirable failure behaviors can occur prior to yielding of the beam itself. For example, we found that while the beam may not fail, and while the data does not suggest such an issue, when loading the beams, the internal joint locations deformed locally, as shown in Figure 12. Because we did not see a drastic change in the slope of the force deflection curves and because the remainder of the beam appeared fine the test could continue. That in mind, however, our data is compounded by this effect, however minimal it may be. Upon removing the load, the joint returned to the correct shape. I did not view this as problematic because the Nomex at the joint is already crushed by designed, so there is little issue with it deforming in the manner it did

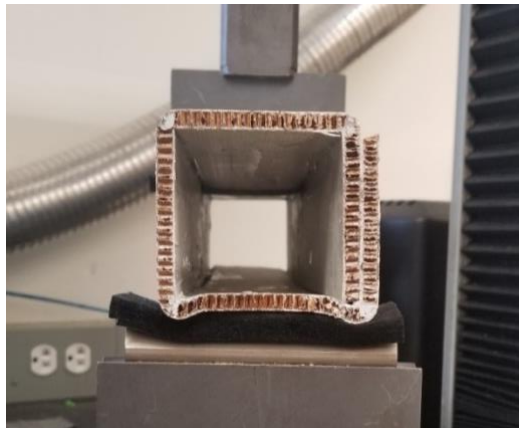


Figure 12: Noncompromising local plastic deformation of the enclosed shape.

Likewise, we found that the top fiberglass facing slightly cracked in a few of the runs, at which point the run was concluded so we would not destroy the section prior to finishing our testing well before the beam itself yielded. Tests in which this occurred were noted, and this data was excluded from linear elastic region calculations. This suggests that for an enclosed sandwich beam, there are two informative metrics of the utmost importance. First, is the flatwise compression of Teklam sheets (see Appendix 2) at 3.26 MPa. This is well below the core yield stresses, max core stresses, and max facing stresses we found from the 3 loading conditions. Essentially, this means that our beam was capable of withstanding forces far beyond what a flat sheet would experience simply in a through thickness compression test. I suspect that this was because at each support and loading point the wall was capable of locally bending out of plane to resist crushing of the Nomex core and because there was no interior forces to simply make the sheet crushed. This means that should we choose to use Teklam in the

design of our vehicle frame, it is important that we do not have interior elements which contact opposing walls (top, bottom; left, right) simultaneously. This may result in local crushing of the Nomex core well below the designed strength of the frame beam element, should the beam come in contact with near point loads in the same location exteriorly (being dropped, sharp rock edges, etc.). Additionally, it may make sense to add more durable facing elements to points of concern, i.e. where interior elements exist, or along vulnerable edges like the bottom of the frame.

Second, is that viable strength of such beams. In the 3-point loading case, we found yielding occurred at ~365 pounds applied to the midspan. Similarly for 4-point quarter case, yielding occurred at ~307 pounds at each loading point, and for the 4-point quarter case, yielding occurred at ~401 pounds on each load point. For a 15 kg vehicle, the average of these values corresponds with a max viable, virtual acceleration due to¹ gravity of ~100m/s². I suspect that the force due to thrust upon descent will likely not be on the order of 10*g, suggesting that a Teklam beam is sufficiently strong to resist bending caused by even the highest anticipated load.

Because we now have a better understand of just how strong a Teklam beam can be, I suggest our lab now focus on either considering methods to limit the complexity of frame elements constructed from Teklam or consider other materials, like carbon fiber, which may be equally strong but easier to work with.

-
- “aeroADD™ Honeycomb Panels: Above and Beyond.” *Collins Aerospace*, www.rockwellcollins.com/Products-and-Services/Commercial-Aviation/Cabin-Interiors/Structures/Honeycomb-Panels/aeroADD.aspx.
- Bonette, Julie. “Engineering Students Seek a Second Win in NASA Competition.” *Thayer School of Engineering at Dartmouth*, 21 Feb. 2020, engineering.dartmouth.edu/news/dartmouth-engineering-again-named-finalists-in-nasas-big-idea-challenge.
- Giglio, M., et al. “Investigations on sandwich core properties through an experimental-numerical approach.” *Composites Part B: Engineering* 43 (2012): 361-374.
- Price, Alexander D. “Cool Robot: Mechanical Design of a Solar-Powered Antarctic Robot.” *Thayer School of Engineering at Dartmouth College*, Trustees of Dartmouth College, 2004.
- Qiao, P, et al. “Impact analysis of fiber reinforced polymer honeycomb composite sandwich Beams.” *Composites Part B: Engineering* 38 (2007): 739-750.
- Roy, R., et al. "Testing and modeling of Nomex™ honeycomb sandwich Panels with bolt insert." *Composites Part B: Engineering* 56 (2014): 762-769.
- “Standard Practice for Determining Sandwich Beam Flexural and Shear Stiffness.” *ASTM Compass*, American Society of Testing and Materials, https://compass.astm.org/EDIT/html_annot.cgi?D7250+16.
- “Standard Test Method for Core Shear Properties of Sandwich Constructions by Beam Flexure.” *ASTM Compass*, American Society of Testing and Materials, compass.astm.org/EDIT/html_annot.cgi?C393.
- “Teklam P/N NE2G102250 Product Data Sheet.” *Rockwell Collins*, beaerospace.com/wp-content/uploads/sites/6/2014/12/NE2G102250.pdf.
- Walker, John. "Flight system architecture for Sorato lunar rover." *The International Symposium on Artificial Intelligence, Robotics and Automation in Space* . 2018¹

Appendix H: Energy Calculations

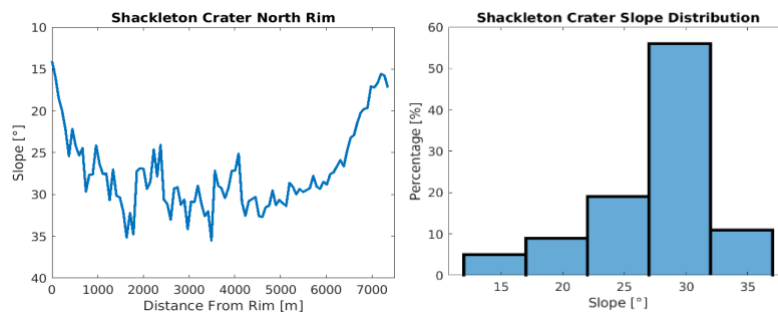
Energy calculations are based on wheel motor sizing and power, housekeeping power, i.e., power required for the electronics and microcontroller, required duration of the mission, and measured energy for the terrestrial prototype on sand.

The terrestrial prototype's as-tested mass is 21.4 kg and energy consumption was measured during a 400 m endurance test as 30 km/kWh while traversing a flat grassy surface at 0.42 m/s. This is based on the total power consumption of the vehicle including the low voltage electronics, which draw 5 to 8 W. On sand (used as our lunar soil analog), instantaneous power was measured while driving straight at 0.46 m/s along a 6.5 m track as 63.7 to 68.8 W. Excluding the housekeeping power of 5 to 8 W results in a projected drive energy of 27 km/kWh for the terrestrial prototype on sand with an average drive power of 56 to 61 W. Scaling this to lunar conditions and the 15 kg mass of the lunar rover, we estimate drive power of 13% of the terrestrial rover or 8 W on level terrain within the PSR. Assuming that the SHREW has scientific instruments active and drawing 3 W of power, total power while exploring is estimated at 24 W.

Lunar electronics and microcontroller are radiation-hardened devices. The IBM RAD6000 is commonly used for space applications and has a housekeeping power of under 7.5 W.² We assume 1 W of housekeeping power per motor controller channel and 1W of power for intermittent communication for a total housekeeping power of 14 W.

The mission profile for the SHREW that disconnects to explore the PSR comprises the upper bound on energy requirements. For this SHREW, we assume the power and energy profile shown in Table G.1. A mission duration of 18.6 hours requires 322 Wh of energy. We size the lunar rover battery for 500 Wh of energy providing 55% reserve energy.

Table H.1.: Mission Energy Profile						
Duration (hours)	Average speed (m/s)	Distance (m)	Mode	Power (W)	Energy (Wh)	Assumptions
5.6	0.3	6000	Idle	13	72.2	SHREW is winched to the bottom of the crater and disconnects. Housekeeping power only.
7.4	0.3	8000	Driving	24	177.8	SHREW explores the PSR. Power budget includes housekeeping power, payload power (4W), and drive power scaled based on terrestrial prototype measurements on sand.
5.6	0.3	6000	Idle	13	72.2	SHREW returns to the caravan, reconnects, and is winched up the slope. Housekeeping power only
Total					322.2	



Based on the LRO LOL DEM, S Pole, 75 Deg (NASA, 2020d)

² https://montcs.bloomu.edu/~bobmon/PDFs/RAD6000_Space_Computers.pdf